Direct observation of the neural computations underlying a single decision

Natalie A Steinemann[1,2,†], Gabriel M Stine[1,2,3†], Eric M Trautmann[1,2,4], Ariel Zylberberg[1,2,‡], Daniel M Wolpert[1,2,‡] & Michael N Shadlen[1,2,5,6,‡,*]

[1] Department of Neuroscience, Columbia University, New York, NY 10027, USA
[2] Zuckerman Mind Brain Behavior Institute, Columbia University, New York, NY 10027, USA
[3] McGovern Institute for Brain Research, Massachusetts Institute of Technology, Cambridge, MA 02139, USA
[4] Grossman Center for the Statistics of Mind, Columbia University, New York, NY 10027, USA
[5] Howard Hughes Medical Institute, Columbia University, New York, NY 10027, USA
[6] Kavli Institute for Brain Science, Columbia University, New York, NY 10027, USA
[†] Co-first authors.
[‡] Co-senior authors.
[*]corresponding author

Neurobiological investigations of perceptual decision-making have furnished the first glimpse of a flexible cognitive process at the level of single neurons (*Shadlen and Newsome, 1996*; *Shadlen and Kiani, 2013*). Neurons in the parietal and prefrontal cortex (*Kim and Shadlen, 1999*; *Romo et al., 2004*; *Hernández et al., 2002*; *Ding and Gold, 2012*) are thought to represent the accumulation of noisy evidence, acquired over time, leading to a decision. Neural recordings averaged over many decisions have provided support for the deterministic rise in activity to a termination bound (*Roitman and Shadlen, 2002*). Critically, it is the unobserved stochastic component that is thought to confer variability in both choice and decision time (*Gold and Shadlen, 2007*). Here, we elucidate this drift-diffusion-like signal on individual decisions by recording simultaneously from hundreds of neurons in the lateral intraparietal cortex (LIP). We show that a single scalar quantity derived from the weighted sum of the population activity represents a combination of deterministic drift and stochastic diffusion. Moreover, we provide direct support for the hypothesis that this drift-diffusion signal is the quantity responsible for the variability in choice and reaction times. The population-derived signals rely on a small subset of neurons with response fields that overlap the choice targets. These neurons represent the integral of noisy evidence from direction-selective neurons within LIP itself. This parsimonious architecture would escape detection by state-space analyses, absent a clear hypothesis.

Introduction

Neural signals in the mammalian cortex are notoriously noisy. They manifest as a sequence of action potentials (spikes) that approximate non-stationary Poisson point processes. Therefore, to characterize the signal produced by a neuron, electrophysiologists typically combine the spike times from many repetitions, or trials, relative to the time of an event (e.g., stimulus onset), to yield the average firing rate of the neuron as a function of time. Such trial-averaged firing rates are the main staple of systems neuroscience. They are the source of knowledge about spatial selectivity (e.g., receptive fields), feature selectivity (e.g., direction of motion, faces vs. other objects), and even cognitive signals associated with working memory, anticipation, attention, motor planning, and decision making. But there is an important limitation.

Trial averages suppress signals that vary independently across trials. In many cognitive tasks, such as difficult decisions, the variable component of the signal is the most interesting, because it is this component that is thought to explain the variable choice and response time. This variability is thought to arise from a decision process that accumulates noisy evidence in favor of the alternatives and terminates when the accumulated evidence for one alternative, termed the decision variable (DV), reaches a terminating bound. The DV is stochastic because the integral of noisy samples of evidence is biased Brownian motion (or drift-diffusion) and this leads to a stochastic choice and response time on each decision. However, the stochastic part of this signal is suppressed by averaging across trials. We will use the term drift-diffusion because it is the expression most commonly applied in models of decision making (*Ratcliff and Rouder, 1998*; *Gold and Shadlen, 2007*), and we will consider the noise part—that is, diffusion—as the signal of interest.

In the setting of difficult perceptual decisions, studied here, bounded drift-diffusion reconciles the relationship between the speed and accuracy of decisions. It also explains the trial-averaged firing rates of neurons in the lateral intraparietal area (LIP) that represent the action used by monkeys to indicate their choice. These firing rate averages show motion-dependent, ramping activity that reflects the direction and strength of motion, consistent with the drift component of drift-diffusion (***Roitman and Shadlen, 2002***). Up to now, however, the diffusion component has not been observed, owing to averaging. There is thus a missing link between the mathematical characterization of the decision process and its realization in neural circuits, leaving open the possibility that drift-diffusion dynamics do not underlie LIP activity (*e.g.* ***Latimer et al., 2015***), or emerge only at the level of the population, without explicit representation by single neurons. We reasoned that these and other alternatives to drift-diffusion could be adjudicated if it were possible to resolve the DV giving rise to a single decision.

This stratagem is now feasible, owing to the development of high-density Neuropixels probes, which are capable of recording from deep sulci in the primate brain. Here we provide the first direct evidence for a drift-diffusion process underlying single decisions. We recorded simultaneously from up to 203 neurons in the lateral intraparietal area (LIP) while monkeys made perceptual decisions about the direction of dynamic random dot motion (***Newsome et al., 1989***; ***Gold and Shadlen, 2007***). Using a variety of dimensionality reduction techniques, we show that a drift-diffusion signal can be detected in such populations on individual trials. Moreover, this signal satisfies the criteria for a DV that controls the choice and reaction time. Notably, the signal of interest is dominated by a small subpopulation of neurons with response fields that overlap one of the choice targets, consistent with earlier single neuron studies (*e.g.,* ***Shadlen and Newsome, 1996***; ***Roitman and Shadlen, 2002***; ***Churchland et al., 2011***; ***Gold and Shadlen, 2007***)

Results

Two monkeys made perceptual decisions, reported by an eye movement, about the net direction of dynamic random dot motion (Fig. 1a). We measured the speed and accuracy of these decisions as a function of motion strength (Fig. 1b, circles). The choice probabilities and the distribution of reaction times (RT) are well described (Fig. 1b, traces) by a bounded drift-diffusion model (Fig. 1c). On 50% of the trials, a brief (100 ms) pulse of weak leftward or rightward motion was presented at a random time. The influence of these pulses on choice and RT further support the assertion that the choices and RTs arose through a process of integration of noisy samples of evidence to a stopping bound (Fig. S1) (***Stine et al., 2020***, ***2023***). In addition to the main task (which we also refer to as choice-RT), the monkeys also performed two control tasks: visually instructed and memory guided saccades to peripheral targets after variable delays and passive viewing of random dot motion (see Methods). These control tasks served to identify, *post hoc*, neurons with response fields that overlap the choice target in the hemifield contralateral to the recording site ($\mathrm{T}_{\mathrm{in}}^{\mathrm{con}}$), neurons with response fields that overlap the other choice target ($\mathrm{T}_{\mathrm{in}}^{\mathrm{ips}}$), and neurons with response fields that overlap the random-dot motion stimulus (M_{in}) (Table 1).

We recorded simultaneously from populations of neurons in area LIP, using newly developed macaque Neuropixels probes while monkeys performed these tasks. The data set comprises eight sessions from two monkeys (1696–2894 trials per session; Table 1). Our primary goal was to characterize decision-related activity accompanying each individual decision. To achieve this, we formed weighted averages from all neurons in the sample population, including those with response fields that did not overlap a choice target or the motion stimulus. We used several strategies to assign this vector of weights, which we refer to as a *coding direction* in the neuronal state space. The projection of the spiking activity from the population of neurons onto the vector of weights gives rise to a scalar function of time, $S^x(t)$, where the superscript x labels the strategy.

We first developed a targeted strategy that would reproduce the well-known coherence-dependent ramping activity evident in the across-trial averages. This strategy applies regression to best approximate a linear ramp, on each trial, i, that terminates with a saccade to the choice-target contralateral to the hemisphere of the LIP recordings. The ramps are defined on the epoch spanning the decision time: from $t_0 = 0.2$ s after motion onset to $t_1 = 0.1$ s before saccade initiation (black lines in Fig. S4). The epoch is motivated by many previous studies (*e.g.*, ***Gold and Shadlen, 2007***, and see below). Each ramp begins at $f_i(t_0) = -1$ and ends at $f_i(t_1) = 1$. The ramp

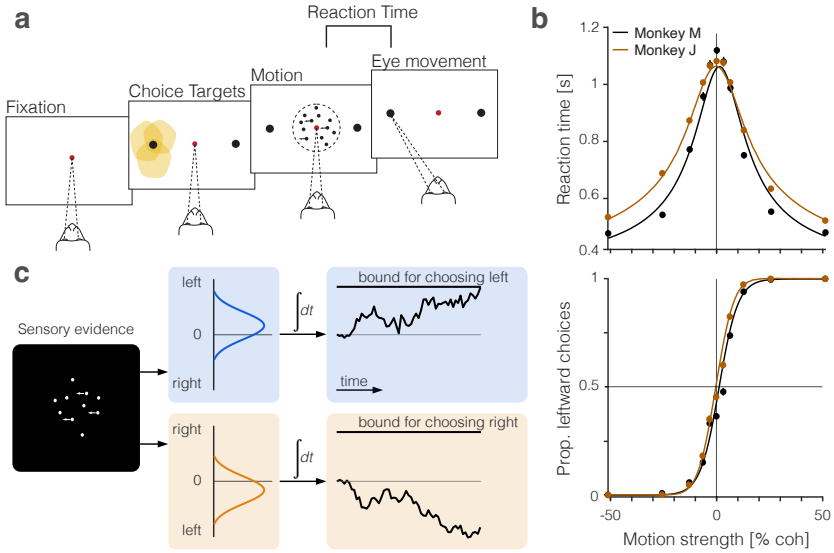

Figure 1. Perceptual decisions are explained by the accumulation of noisy evidence to a stopping bound. a, Random dot motion discrimination task. The monkey fixates a central point. After a delay, two peripheral targets appear, followed by the random dot motion. When ready, the monkey reports the net direction of motion by making an eye movement to the corresponding target. Yellow shading indicates the response fields of a subset of neurons in area LIP that we refer to as T_{in} neurons (*target in response field*). **b,** Mean reaction times (top) and proportion of leftward choices (bottom) plotted as a function of motion strength and direction, indicated by the sign of the coherence: positive is leftward. Data (circles) are from all sessions from monkey M (black, 9684 trials) and monkey J (brown, 8142 trials). Solid lines are fits of a bounded drift-diffusion model. **c,** Drift-diffusion model. The decision process is depicted as a race between two accumulators: one integrating momentary evidence for left; the other for right. The momentary samples of evidence are sequential samples from a pair of negatively correlated ($\rho = -0.71$) Normal distributions. The decision is terminated when one accumulator reaches its positive bound. The example depicts leftward motion leading to a leftward decision.

---

approximates the expectation—conditional on the choice and response time—of the deterministic components of the drift-diffusion signal which can incorporate (*i*) the deterministic drift, (*ii*) a time-dependent but evidence-independent urgency signal (***Drugowitsch et al., 2012***), and (*iii*) a dynamic bias signal (***Hanks et al., 2011***). It can also be viewed as an approximation to firing rates averaged across trials and grouped by contraversive choice and RT quantile (*e.g.*, ***Roitman and Shadlen, 2002***, see also Fig. S2). Importantly, the fit is not guided by an assumption of an underlying diffusion process. That is, the ramp coding direction is agnostic to the underlying processes whose averages approximate ramps. The weights derived from these regression fits specify a ramp-coding direction in the state space defined by the population of neurons in the session. The single-trial signal, $S^{\text{ramp}}(t)$, is rendered as the projection of the population firing rates onto this coding direction.

The left side of Fig. 2a shows single-trial activity rendered by this strategy. The right side of the figure shows the averages of the single-trial responses grouped by signed coherence and aligned to motion onset or response time (saccade initiation). These averaged traces exhibit features of the firing rate averages in previous studies of single neurons in LIP (e.g., see ***Roitman and Shadlen, 2002***; ***Gold and Shadlen, 2007***, and Fig. S2). They begin to diverge as a function of the direction and strength of motion ∼200 ms after the onset of motion and they converge near the time of the monkey's saccadic response to the target contralateral to the recording site. They maintain coherence dependence until ∼100 ms before the initiation of saccades to the left (contralateral) choice target, whereas they retain this dependence through the initiation of saccades to the right (ipsilateral) target.

We complemented this regression strategy with Principal Components Analysis (PCA) and use the first PC (PC1), which explains 45 ± 3% of the variance (mean ± s.e. across sessions) of the activity between 200 and 600 ms from motion onset (see Methods). This coding direction renders single trial signals, $S^{\text{PC1}}(t)$ (Fig. 2b). In a third strategy, we consider the mean activity of neurons with response fields that overlapped the contralateral choice

target (T_{in}^{con} neurons), which were the focus of previous single-neuron studies (e.g., ***Shadlen and Newsome, 1996***; ***Platt and Glimcher, 1999***; ***Roitman and Shadlen, 2002***). In those studies, the task was modified so that one of the choice targets was placed in the neural response field, whereas here we identify neurons *post hoc* with response fields that happen to overlap the contralateral choice target. This difference probably accounts for the lower firing rates of the T_{in}^{con} neurons studied here. Fig. 2c shows single-trial and across-trial averages from these T_{in}^{con} neurons. They too render signals, $S_{Tin}^{con}(t)$, similar to those derived from the full population. The T_{in}^{con} neurons thus furnish a third coding direction defined by a vector of identical positive weights assigned to all T_{in}^{con} neurons and 0 for all other neurons in the population. The emboldened single-trial traces in Fig. 2 *left* correspond to the same trials rendered by the three coding directions. It is not difficult to tell which are the corresponding traces, an observation that speaks to their similarity, and the same is true for the averages. We will expand on this observation in what follows.

The averages show the deterministic *drift* component of the hypothesized drift-diffusion process, with the slope varying monotonically with the signed motion strength (Fig. 2 *right*). The rise begins to saturate as a consequence of the putative termination bound—a combination of dropout of trials that are about to terminate and the effect on the distribution of possible diffusion paths imposed by the very existence of a stopping bound. This saturation is evident earlier on trials with stronger motion, hence shorter RT, on average. The positive buildup rate on the 0% coherence motion represents the time-dependent, evidence-independent signal that is thought to reflect the cost of time. It leads to termination even if the evidence is weak, equivalent to collapsing stopping bounds in drift-diffusion models (***Drugowitsch et al., 2012***). Removal of this *urgency* signal, $u(t)$, from the non-zero coherence traces renders the positive and negative coherence averages symmetric relative to zero on the ordinate (Fig. S5).

The single-trial responses in Fig. 2 do not look like the averages but instead approximate drift-diffusion. We focus on the epoch from 200–500 ms from motion onset—that is, the first 300 ms of the period in which the averages reflect the integration of evidence. Some traces are cut off before the end of the epoch because a saccade occurred 100 ms later on the trial. However, most 0% coherence trials continue beyond 500 ms (median RT > 600 ms). The single-trial traces do not rise monotonically as a function of time but meander and tend to spread apart from each other vertically as a function of time. For unbounded diffusion, the variance would increase linearly, but as just mentioned, the existence of an upper stopping bound and the limited range of firing rates (*e.g.*, non-negative) renders the function sublinear at later times (Fig. 3a). The autocorrelation between an early and a later sample from the same diffusion trace is also clearly specified for unbounded diffusion. The theoretical values shown in Fig. 3b & c are the autocorrelations of unbounded diffusion processes that are smoothed identically to the neural signals (see Methods and Appendix). The autocorrelations in the data follow a strikingly similar pattern. These observations support the assertion that the coherence-dependent (ramp-like) firing rate averages observed in previous studies of area LIP are composed of stochastic drift-diffusion processes on single trials.

Single-trial drift-diffusion signals control the choice and decision time

We next evaluate the hypothesis that the drift-diffusion signal, $S^x(t)$, is the decision variable that controls the choice and response time. We have identified several coding directions that produce candidate DVs, and as we will see below, there are also other coding directions of interest that can be derived from the population. Therefore, one might wonder whether it is sensible to assume that the DV can be approximated by a scalar measure arising from a single coding direction as opposed to a higher dimensional representation. Two decoding exercises are adduced to support the assumption.

We constructed a logistic decoder of choice using each neuron's spike counts in 50 ms bins between 100 and 500 ms after motion onset. As shown in Fig. 4a, this *What*-decoder (orange) predicts choice as accurately as a decoder of simulated data from a drift-diffusion model (black) using parameters derived from fits to the monkeys' choice and RT data (see Methods). The simulation establishes a rough estimate of the decoding accuracy that can be achieved, given the stochastic nature of the choice, were we granted access to the drift-diffusion signal that actually determines the decision. In this analysis, the decoder can use a different vector of weights at each point in time (*time-dependent* coding directions; see ***Peixoto et al., 2021***). However, if the representation of the

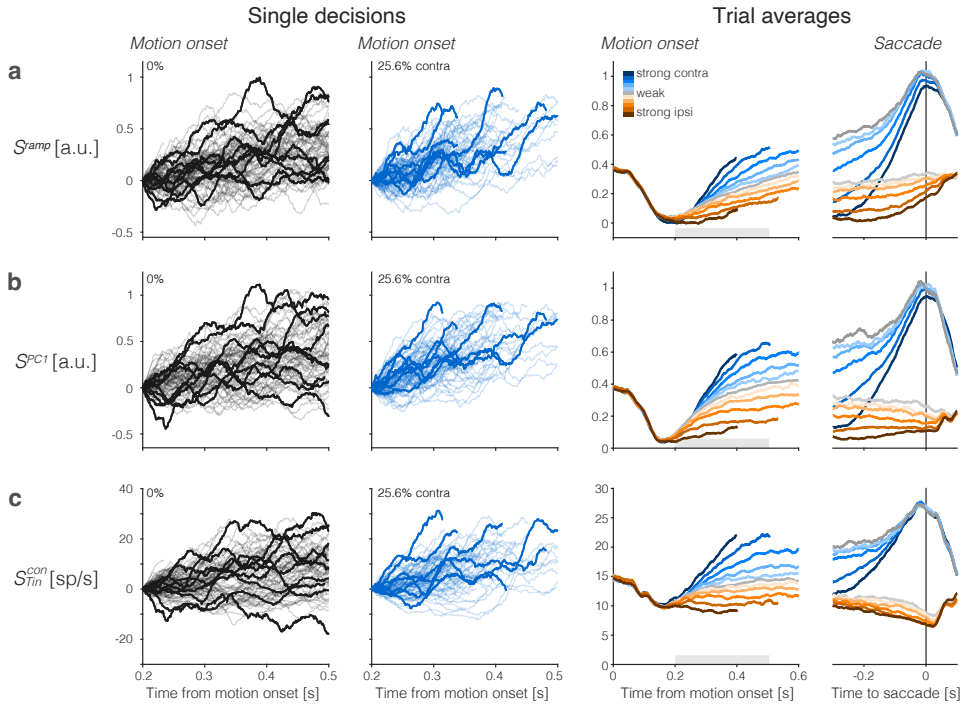

Figure 2. Population responses from LIP approximate drift-diffusion. Rows show three types of population averages. The left columns show representative single-trial firing rates during the first 300 ms of evidence accumulation using two motion strengths: 0% and 25.6% coherence toward the left (contralateral) choice target. We highlight a number of trials with thick traces and these are the same trials in each of the rows. The right columns show the across-trial average responses for each coherence and direction. Motion strength and direction are indicated by color (legend) and aligned to motion onset (left) and saccade initiation (right). The gray bars under the motion-aligned averages indicate the 300 ms epoch used in the display of the single-trial responses (left panels). It begins when LIP first registers a signal related to the strength and direction of motion. Except for saccade-aligned response, trials are cut off 100 ms before saccade initiation. Error trials are excluded from the saccade-aligned averages, only. **a,** Ramp coding direction. The weight vector is established by regression to ramps from -1 to $+1$ over the period of putative integration, from 200 ms after motion onset to 100 ms before saccade initiation (see Fig. S4). Only trials ending in left (contralateral) choices are used in the regression. **b,** First principal component (PC1) coding direction. **c,** Average firing rates of the subset of neurons that represent the left (contralateral) target. The weight vector consists of $\frac{1}{N}$ for each of the N $\mathrm{T}^{\mathrm{con}}_{\mathrm{in}}$ neurons and 0 for all other neurons. Note the similarity of both the single-trial traces and the response averages produced by the different weighting strategies.

decision variable in LIP is one-dimensional, then a decoder trained at one time should perform well when tested at a different time. The red curve in Fig. 4a shows the performance of a *What*-decoder with a *fixed training-time* that was 450 ms after motion onset (red arrow). This decoder performs nearly as well as the decoder trained at each time bin. The heatmap (Fig. 4b) generalizes this observation. It shows two main features for all times $250 < t < 500$ ms (dashed box). First, unsurprisingly, for a *What* choice decoder trained on data at one time $t = x$ the predictions improve as the testing time advances (the decoding accuracy increases along any vertical) as the accumulated evidence increases. Second, and more importantly, decoders tested at time $t = y$ perform similarly independent of when they were trained (there is little variation in decoding accuracy along any horizontal). This observation suggests that a single vector of weights may suffice to decode the choice from the population response.

The second decoder is trained to predict whether a saccade to the contralateral choice target will be initiated in the next 150 ms. This *When*-decoder is trained by logistic regression to predict a binary output which is 1 at all time-points that are within 150 ms of an upcoming saccade and 0 elsewhere (Fig. S7). We validated the When-decoder by computing the area under an ROC (AUC) using the held-out (odd) trials (mean AUC over all time points: 0.84), but this is tangential to our goal. Although the *When*-decoder was trained only to predict the time of saccades, our rationale for developing this decoder was to test whether the *When* coding direction can be used to predict the

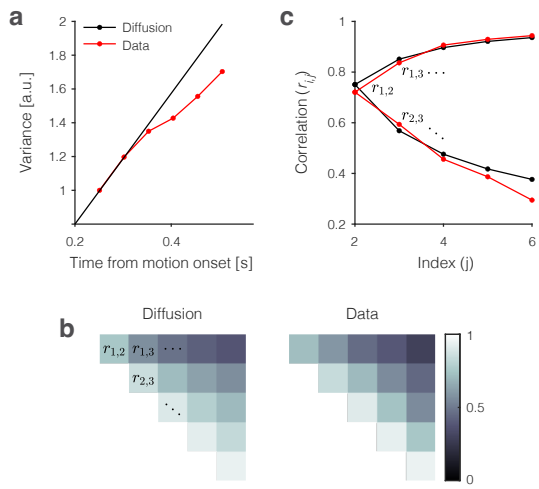

Figure 3. Variance and autocorrelation of the single trial signals. The analyses here are based on samples of S^{ramp} at six time points during the first 300 ms of putative integration, using all 0% and ±3.2% coherence trials ($N = 5927$). Samples are separated by the width of the boxcar filter (51 ms), beginning at $t_1 = 225$ ms. The smoothed traces are detrended by the mean across trials and the value of $S^{\text{ramp}}(t_0 = 0.2)$ on each trial. **a,** Variance increases as a function of time. The measure of variance is normalized so that it is 1 for the first sample. **b**, Autocorrelation of samples as a function of time and lag approximate the values expected from diffusion. The upper triangular portion of the 6×6 correlation matrix for unbounded diffusion ($r_{i,j}$ is represented by brightness). The values from the data (S^{ramp}) are similar (right). **c** Nine of the 15 autocorrelation terms in **b** permit a more direct comparison of theory and data. The lower limb of the C-shaped function shows the decay in $r_{i,j}$ as a function of lag $(j - i)$. This is the top row of **b**. The upper limb shows the increase in $r_{i,j}$ as a function of time (for fixed lag). This is the lower diagonal in **b**. Note that the autocorrelations incorporate a free parameter, $\phi \leq 1$, that serves to correct for an unknown fraction of the measured variance that is not explained by diffusion (see Methods).

---

choice. The green trace in Fig. 4a shows the accuracy of $S^{\text{When}}(t)$ to predict the choice. The performance is almost identical to the fixed training-time choice decoder, despite being trained on a temporal feature of trials ending in the same left choice.

This feat is explained by the similarity of signals produced by the *When*- and other coding directions. Note the similarity of the trial averaged S^{When} signals displayed in Fig. 4c to those in Fig. 2 (see also Fig. S8a, right). Indeed, the cosine similarity between the *When* and *Ramp* coding directions is 0.67 ± 0.03 (Fig. 4d). In light of this, it is not surprising that the weighting vectors derived from both the *What*- and *When*-decoders also render single-trial drift-diffusion traces that resemble each other and those rendered by other coding directions (Fig. 4e). Together these analyses support the assertion that the DV is likely to be captured by a single dimension, consistent with ***Ganguli et al.*** (***2008***).

If the one-dimensional signals, $S^x(t)$, approximate the decision variable, they should explain the variability of choice and reaction time for trials sharing the same direction and motion strength. Specifically, (*i*) early samples of $S^x(t)$ should be predictive of choice and correlate inversely with the RT on trials that result in contraversive (leftward) choices, (*ii*) later samples ought to predict choice better and correlate more strongly (negatively) with RT than earlier samples, and (*iii*) later samples should contain the information present in the earlier samples and thus mediate (i.e., reduce the leverage) of the earlier samples on choice and RT. Each of these predictions is borne out by the data.

The analyses depicted in Fig. 5 allow us to visualize the influence of the single trial signals, $S^x(t)$, on the choice and RT on that trial. We focus on the early epoch of evidence accumulation (200–550 ms after random dot motion onset) and restrict the analyses to decisions with RT $\geq$ 670 ms ($\sim$ 83% of the eligible trials; see Methods). Larger values of $S^x(t)$ are associated with a larger probability of a left (contraversive) choice and a shorter RT, hence negative correlation between $S^x(t)$ and RT. We use the term, leverage, to describe the strength of both of these associations. The leverage on choice (Fig. 5a, black traces) is the contribution of $S^x(t)$ to the log odds of

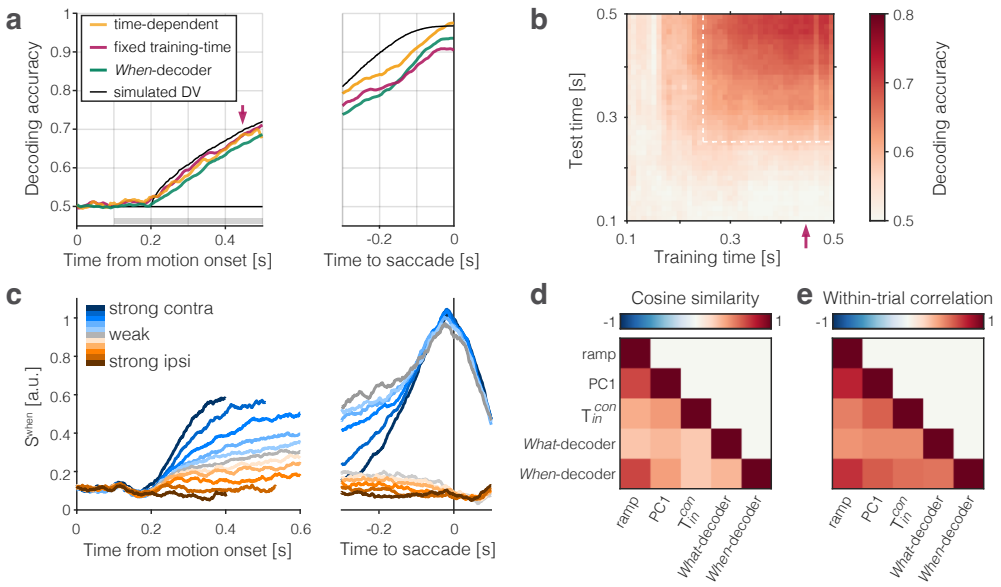

Figure 4. The population signal predictive of choice and RT is approximately one-dimensional. Two binary decoders were trained to predict the choice (*What*-decoder) and its time (*When*-decoder) using the population responses in each session. The *When*-decoder predicts whether a saccadic response to the contralateral target will occur in the next 150 ms, but critically, its accuracy is evaluated based on its ability to predict choice. **a,** Choice decoding accuracy plotted as a function of time from motion onset (left) and time to saccadic choice (right). Values are averages across sessions. The *What*-decoder is either trained at the time point at which it is evaluated (time-dependent decoder, orange) or at the single time point indicated by the red arrow ($t = 450$ ms after motion onset; *fixed training-time* decoder, red). Both training procedures achieve high levels of accuracy. The *When*-decoder is trained to capture the time of response only on trials terminating with a left (contraversive) choice. The coding direction identified by this approach nonetheless predicts choice (green) nearly as well as the *fixed training-time What*-decoder. The black trace shows the accuracy of a *What*-decoder trained on simulated signals using a drift-diffusion model that approximates the behavioral data in Fig. 1. Shaded bar shows the epoch depicted in the next panel. **b,** The heat map shows the accuracy of a decoder trained at times along the abscissa and tested at times along the ordinate. Time is relative to motion onset (gray shading in **a**). In addition to training at $t = 450$ ms, the decoder can be trained at any time from $250 < t < 500$ ms and achieve the same level of accuracy when tested at any single test time. The orange and red traces in **a** correspond to the main diagonal ($x = y$) and the column marked by the red arrow, respectively. **c,** Trial-averaged activity rendered by the projection of the population responses along the *When* coding direction, S^{When}. Same conventions as in Fig. 2. **d,** Cosine similarity of five coding directions. The heatmap shows the mean values across the sessions, arranged like the lower triangular portion of a correlation matrix. The main diagonal is by definition 1. All but one of the 80 unique pairs (10×8 sessions) are greater than zero ($p < 10^{-28}$, t-test, $\mathscr{H}_0$: mean cosine similarity is 0). **e,** Correlation of single-trial diffusion traces. The Pearson correlations are calculated from ordered pairs of $\{S^x(t_i), S^y(t_i)\}$, where i is the sample time of the detrended signals. The detrending removes trial-averaged means for each signed coherence, leaving only the diffusion component.

---

a left choice, after accounting for the motion strength and direction (i.e., the coefficients, $\beta_1(t)$ in Eq. 7). The leverage on RT (Fig. 5b) is the Pearson correlation between $S^x(t)$ and the RT on that trial, after accounting for the effect of motion strength and direction on S^x and RT (See Methods). The leverage is evident from the earliest sign of evidence accumulation, 200 ms after motion onset, and its magnitude increases as a function of time, as evidence accrues (Fig. 5, *top*). The filled circle to the right of the traces in each graph shows the leverage of S^x at $t = 550$ ms, which is 120 ms before any of the included trials have terminated. Both observations are consistent with the hypothesis that S^x represents the integral of noisy evidence used to form and terminate the decision.

Importantly, the leverage at earlier times is mediated by the later sample at $t = 550$ ms. The green traces in all the graphs show the remaining leverage, once this later sample is allowed to explain the choice or RT. This is achieved by including an additional term in the logistic regression or the partial correlation, conditional on $S^x(t = 0.55)$. The stark decrease in leverage is consistent with one-dimensional diffusion in which later values of the signal contain the information in the earlier samples plus what has accrued in the interim. Had we recorded from all the neurons that represent the DV, we would expect the mediation to be complete (e.g., partial correlation = 0).

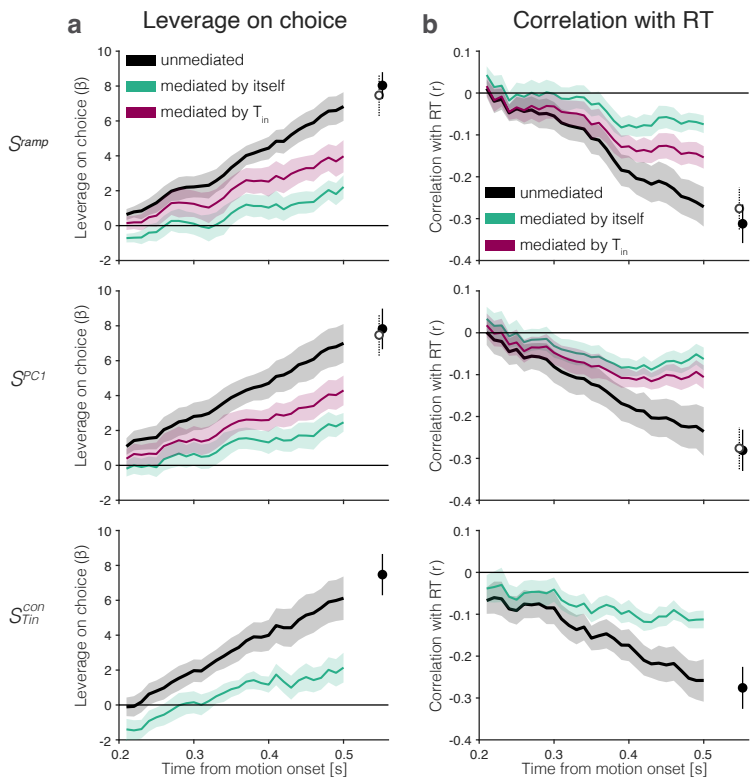

Figure 5. The drift-diffusion signal is the decision variable. The graphs show the leverage of single-trial drift-diffusion signals on choice and RT using only trials with RT ≥ 0.67 s. Rows correspond to the same coding directions as in Fig. 2. The graphs also demonstrate a reduction of the leverage of the samples at $t \leq 0.5$ s by a later sample of the signal at $t = 0.55$ s. **a,** Leverage of single-trial drift-diffusion signals on choice. Leverage is the value of β_1, the coefficient that multiplies $S(t)$ in the GLM to predict choice (Eq. 7). The black traces show the increase in leverage as a function of time. Filled symbols show the leverage at $t = 0.55$ s. The green curve shows the leverage when the later sample is included in the GLM (mediation by later sample of the row signal). Open symbols show the leverage of $S^{\text{con}}_{\text{Tin}}$ at $t = 0.55$ s (same value as the filled symbol in *bottom row*). The red curves (top and middle rows) show the leverage of the signal when the later sample of $S^{\text{con}}_{\text{Tin}}$ is included in the GLM (mediation by the later sample of $S^{\text{con}}_{\text{Tin}}$). **b,** Leverage of single-trial drift-diffusion signals on response time. Leverage is the correlation between $S(t)$ and RT. Same conventions as in **a**; the green and red traces are partial correlation of $S(t)$ and RT given S^{ramp}, (top), along PC1 (S^{PC1}, middle) and of $\text{T}^{\text{con}}_{\text{in}}$ neurons ($S^{\text{con}}_{\text{Tin}}$, bottom). Black traces signify the unmediated relationship and green and red traces the leverage after accounting for activity at $t = 0.55$ ms of the signal itself (filled symbol) or S_{Tin} activity (open symbol), respectively. Error bars signify s.e.m across sessions.

However, our recorded population is only a fraction of the entire population.

There is one additional noteworthy observation in Fig. 5 that highlights the importance of the $\text{T}^{\text{con}}_{\text{in}}$ neurons. The top and middle rows (S^{ramp} and S^{PC1}) contain a second, open symbol, which is simply a copy of the filled symbol from the bottom row ($S^{\text{con}}_{\text{Tin}}$). The red traces show mediation of S^{ramp} and S^{PC1} by the sample, $S^{\text{con}}_{\text{Tin}}(t = 0.55)$. This signal, carried by 9–21% of the neurons mediates signals produced by the full population of 54–203 neurons nearly as strongly as S^{ramp} and S^{PC1} mediate themselves. The observation suggests that minimal leverage is gained by sophisticated analyses of the full neuronal state space compared to a simple average of $\text{T}^{\text{con}}_{\text{in}}$ neurons. This is both reassuring and disquieting: reassuring because the $\text{T}^{\text{con}}_{\text{in}}$ neurons compose the dominant projection from LIP to the portions of the superior colliculus and the frontal eye field involved in the generation of contraversive saccades (***Paré and Wurtz, 1998***; ***Ferraina et al., 2002***); disquieting because the functional relevance of these neurons is not revealed by the other coding directions. The weights assigned to the $\text{T}^{\text{con}}_{\text{in}}$ neurons span all percentiles (mean IQR: 49–96; mean 71st percentile, $AUC = 0.74 \pm 0.05$) in the ramp coding direction. They contribute disproportionately to PC1 and the *What*- and *When*- decoders but not enough to stand out based on their weights. Indeed, the ability to predict that a neuron is $\text{T}^{\text{con}}_{\text{in}}$ from its weight or percentile is remarkably poor (Fig. S3).

These observations support the idea that the single-trial signals, S^{ramp}, S^{PC1} and $S^{\text{con}}_{\text{Tin}}$, approximate the DV used by the monkey to make its decision. They are not unique. In Fig. S9 we show that the S^{What} and S^{When} coding directions achieve qualitatively similar results. Moreover, a late sample from $S^{x}(t)$ mediates the earlier correlation with RT and choice of signals rendered by other coding directions, $S^{y}(t)$, at earlier times (Fig. S9). Such cross-mediation is consistent with the high cosine similarity of the coding directions (Fig. 4e). The observation suggests that the decision variable is a prominent signal in LIP, discoverable by a variety of strategies, and consistent with the idea that it is one-dimensional.

A representation of momentary evidence in area LIP

Up to now, we have focused our analyses on resolving the DV on single trials, paying little attention to its formation. The drift-diffusion signal approximates the accumulation, or integral, of the noisy momentary evidence—a signal approximating the difference in the firing rates of direction-selective (DS) neurons with opposing direction preferences (e.g, in area MT; ***Britten et al., 1996***). DS neurons, with properties similar to neurons in MT, have also been identified in area LIP (***Freedman and Assad, 2006***; ***Shushruth et al., 2018***; ***Fanini and Assad, 2009***; ***Bollimunta and Ditterich, 2012***), where they are proposed to play a role in motion categorization (***Freedman and Assad, 2011***). We hypothesize that such neurons might participate in routing information from DS neurons in MT/MST to those in LIP that contain a choice-target in their response fields.

We identified such direction selective neurons using a passive motion viewing task (Fig. 6a-b, left). Neurons preferring leftward or rightward motion constitute 5–10% of the neurons in our sample populations Table 1. Fig. 6 shows the average firing rates of 55 leftward-preferring neurons ($\text{M}^{\text{left}}_{\text{in}}$, Fig. 6a) and 26 rightward-preferring neurons ($\text{M}^{\text{right}}_{\text{in}}$, Fig. 6b) during passive motion viewing and during the choice-RT task. The separation of the two traces in the passive viewing task is guaranteed because we used this task to identify the DS neurons. It is notable, however, that the DS is first evident $\sim$ 100 ms after the onset of random dot motion, and this latency is also apparent in mean firing rates grouped by signed coherence during decision making (Fig. 6a,b *right*). The activity of DS neurons is modulated by both the direction and strength of motion. However, unlike the T_{in} neurons, the traces associated with different motion strengths are mostly parallel to one another and do not reach a common level of activity before the saccadic eye movement (i.e., they do not signal decision termination).

In addition to their shorter onset latency, the direction-selectivity of M_{in} neurons precedes the choice-selectivity of $\text{T}^{\text{con}}_{\text{in}}$ neurons by $\sim$100 ms (Fig. 6c). The responses bear similarity to DS neurons in area MT. Such neurons are known to exhibit choice-dependent activity insofar as they furnish the noisy evidence that is integrated to form the decision (***Britten et al., 1996***; ***Shadlen et al., 1996***). We computed putative single trial direction signals by averaging the responses from the left- and right-preferring DS neurons, respectively. The resulting signals, $S^{\text{left}}_{\text{Min}}(t)$ and $S^{\text{right}}_{\text{Min}}(t)$, have weak leverage on choice, but the leverage does not increase as a function of time (Fig. 6d, *left*). This is what would be expected if the M_{in} neurons represent the noisy momentary evidence as opposed to the accumulation thereof (***Mazurek et al., 2003***). We failed to detect a correlation between RT and either S_{Min} signal (Fig. 6d, *right*). This is surprising, but it could be explained by lack of power—a combination of small numbers of M_{in} neurons, narrow sample windows (50 ms boxcar) and the focus on the long RT trials. To support this assertion, we found a weak but statistically significant negative correlation between RT and the difference in leftward vs. rightward signals, averaged over the epoch $0.1 \leq t \leq 0.4$ s from motion onset ($p = 0.0004$; $\mathscr{H}_0 : \rho \geq 0$, see Methods).

We considered the hypothesis that these DS signals are integrated by the $\text{T}^{\text{con}}_{\text{in}}$ neurons to form the DV. The heatmap in Fig. 6d supports this hypothesis. On each trial, we formed the ordered pairs, $\{x, y\}$, where $x = \tilde{S}^{\text{left}}_{\text{Min}}(t_x) - \tilde{S}^{\text{right}}_{\text{Min}}(t_x)$ and $y = \tilde{S}^{\text{con}}_{\text{Tin}}(t_y)$. The tilde in these expressions indicates the use of standardized residual values, for each signed motion strength. The heatmap shows the correlation of these quantities across trials. If the hypothesis is true, the correlations should be positive for $t_y > t_x$ when $t_x > 100$ ms and $t_y > 200$ ms, and if the operation approximates integration, the level of correlation should be consistent at all lags, $t_y - t_x > 100$ ms. The correlations are significant in the epoch of interest, and they differ significantly from the average correlations in the rest of the graph (i.e., $t_x < 100$, $t_y < 200$, or $t_y < t_x$; $p < 0.0001$, permutation test). Although correlative, the observation is

consistent with the idea that evidence integration occurs within area LIP, rather than inherited from another brain area (***Zhang et al., 2022***; ***Bollimunta and Ditterich, 2012***).

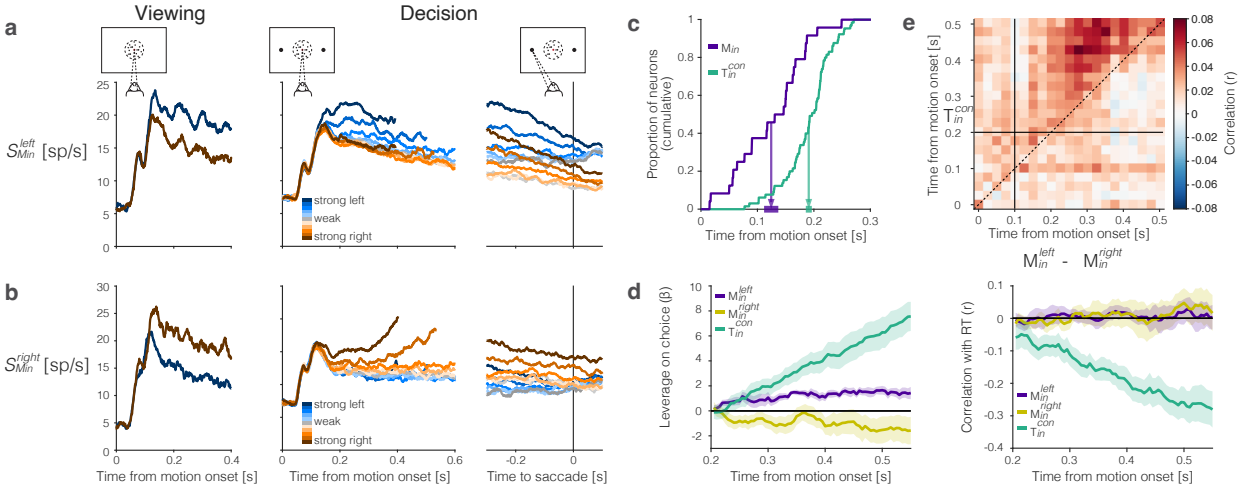

Figure 6. The representation of momentary evidence in area LIP. a, Leftward preferring neurons. (*left*) Response to strong leftward (blue) and rightward (brown) motion during passive viewing. Traces are averages over neurons and trials. The neurons were selected for analysis based on this task, hence the stronger response to leftward is guaranteed. Note the short latency visual response to motion onset followed by the direction-selective (DS) response beginning ∼100 ms after motion onset. (*right*) Responses during decision aligned to motion onset and saccadic response. Response averages are grouped by direction and strength of motion (color legend). The neurons retain the same direction preference during passive viewing and decision-making. The responses are also graded as a function of motion strength. **b,** Rightward preferring neurons. Same conventions as **a**. **c,** Cumulative distribution of the times at which individual neurons start showing evidence-dependent activity. Evidence dependence emerges earlier in $\mathrm{M}_{\mathrm{in}}^{\mathrm{left}}$ and $\mathrm{M}_{\mathrm{in}}^{\mathrm{right}}$ neurons (purple) than $\mathrm{T}_{\mathrm{in}}^{\mathrm{con}}$ neurons (green). Arrows indicate the mean onset of evidence-dependent activity in each signal. The markers at the end of the arrows show the s.e.m. across neurons. **d,** Correlation between the neural representation of motion evidence—the difference in activity of neurons selective for leftward and rightward motion $\left(\mathrm{M}_{\mathrm{in}}^{\mathrm{left}} - \mathrm{M}_{\mathrm{in}}^{\mathrm{right}}\right)$—and the neural representation of the decision variable $\left(S_{\mathrm{Tin}}^{\mathrm{con}}\right)$ across different time points and lags. Horizontal and vertical lines indicate the onset of evidence-dependent activity in each signal. Positive correlations in the upper left triangle indicate that the decision variable at a time point is correlated with earlier activity of the evidence signal. **e,** Leverage of neural activity on choice for $\mathrm{T}_{\mathrm{in}}^{\mathrm{con}}$ (green), $\mathrm{M}_{\mathrm{in}}^{\mathrm{left}}$ (purple) and $\mathrm{M}_{\mathrm{in}}^{\mathrm{right}}$ (yellow) neurons. **f,** Same as **e** for the correlation between neural activity and reaction time. The absence of negative correlation is explained by insufficient power (see Methods).

Discussion

We have observed a neural representation of the stochastic process that gives rise to a single decision. This is the elusive drift-diffusion signal that has long been thought to determine the variable choice and response time in the perceptual task studied here. The signal was elusive because it is the integral of noisy momentary evidence, hence stochastic, and undetectable in the firing rates when they are computed as averages over trials. The averages preserve the ramp-like *drift* component, leaving open the possibility that the averages are composed of other stochastic processes (*e.g.,* ***Latimer et al., 2015***; ***Cisek et al., 2009***). By providing access to populations of neurons in LIP, macaque Neuropixels probes (***Trautmann et al., 2023***) allowed us to resolve, for the first time, the evolution of LIP activity during a single decision.

The present finding establishes that the ramp-like averages arise from drift-diffusion on single trials, and this drift-diffusion signal arbitrates the choice and RT on that trial. We used a variety of strategies to assign a weight to each neuron in the population such that the vector of weights defines a coding direction in neuronal state space. The weighted averages render population firing rate signals on single trials. Our experience is that any method of assigning the weights that captures a known feature of evidence accumulation (or its termination in a saccadic choice) reveals drift-diffusion on single trials, and this also holds for data-driven, hypothesis-free methods such as PCA. This is because the actual dimensionality of the DV is effectively one—a scalar function of time that connects the visual representation of a choice target to the saccadic choice (***Ganguli et al., 2008***). Thus a weighting established by training a decoder at time $t = \tau$ to predict the monkey's choice performs nearly as well when tested at times other than the time the decoder was trained on (*i.e.*, $t \neq \tau$; Fig. 4).

The different strategies for deriving coding directions lead to different weight assignments, but the coding directions are linearly dependent (Fig. 4e). They produce traces, $S(t)$, that are similar (Fig. 4f) and suggestive of drift-diffusion. Traces accompanying trials with the same motion coherence meander and spread apart at a rate similar to diffusion (*i.e.*, standard deviation proportional to $\sqrt{t}$), and they exhibit a pattern of autocorrelation, as a function of time and lag, consistent with diffusion (Fig. 3). The calculations applied in the present study improve upon previous applications (*e.g.* ***Churchland et al., 2011***; ***de Lafuente et al., 2015***; ***Shushruth et al., 2018***) by incorporating the contribution of the smoothing to the autocorrelations. The modest departures from theory are explained by the fact that the accumulations are bounded. The upper bound limits the spread of the single-trial traces. The fact that spike rates must be non-negative (a *de facto* lower reflecting bound) accelerates the decay in autocorrelation as a function of lag.

The single-trial signals, $S_i^x(t)$, approximate the DV that gives rise to the choice and decision time on the trial (Fig. 5 and Fig. S9). Support for this assertion is obtained using a conservative assay, which quantifies the leverage of the first 300 ms of the signal's evolution on decision outcomes—choice and RT—occurring at least 670 ms after motion onset. Naturally, the signals do not explain all the variance of these outcomes. The sample size is limited to N randomly selected, often weakly correlated neurons. The sample size and correlation are especially limiting for the $\mathrm{T}_{\mathrm{in}}^{\mathrm{con}}$ neurons ($\mathbb{E}(r) = 0.067 \pm 0.0036$). In addition, because they are identified *post hoc*, many have response fields that barely overlap the choice target. Presumably, that is why their responses are weak compared to previous single-neuron studies in which the choice targets were centered in the response field by the experimenter. Yet even this noisy signal, $S_{\mathrm{Tin}}^{\mathrm{con}}$, mediates signals produced by coding directions using the entire population (Fig. 5).

The $\mathrm{T}_{\mathrm{in}}^{\mathrm{con}}$ neurons were the first to be identified as a plausible candidate neural representation of the decision variable, based on firing rate averages (***Shadlen and Newsome, 1996***; ***Platt and Glimcher, 1999***). This neural type is also representative of the LIP projection to the region of the superior colliculus (SC) that represents the choice target (***Paré and Wurtz, 1998***). In a companion study by ***Stine et al.*** (***2023***) we show that the SC is responsible for cessation of integration in LIP. Features of the drift-diffusion signal from the $\mathrm{T}_{\mathrm{in}}^{\mathrm{con}}$ neurons are correlated with bursting events in corresponding populations of $\mathrm{T}_{\mathrm{in}}^{\mathrm{con}}$ neurons in the SC, including the final saccadic burst that ends the decision with a saccade to the contralateral choice target. ***Stine et al.*** (***2023***) also show that inactivation of $\mathrm{T}_{\mathrm{in}}^{\mathrm{con}}$ neurons in the SC has little effect on $S_{\mathrm{Tin}}^{\mathrm{con}}$ signals in LIP.

Previous studies of LIP using the random dot motion task focused primarily on the $\mathrm{T}_{\mathrm{in}}^{\mathrm{con}}$ neurons (*cf.* ***Meister et al., 2013***). It was thus unknown whether and how other neurons contribute to the decision process. The Neuropixels probes used in the present study yield a large and unbiased sample of neurons. Many of these neurons have response fields that overlap one of the two choice targets, but the majority have response fields that overlap neither the choice targets nor the random dot motion. Our screening procedures (delayed saccades and passive motion viewing tasks) do not supply a quantitative estimate of their spatial distribution. It is worth noting that neurons that had response fields that overlapped neither of the two choice targets are assigned nonzero weights in the What- and When-decoders, and yet removal of the task-related neurons that represent the choice targets and motion (i.e., T_{in} and M_{in}) nearly abolishes decoding accuracy even after retraining (Fig. S6). What accuracy the decoder achieves is likely explained by neurons with weak responses that simply failed to meet our criterion for inclusion in the T_{in} and M_{in} categories (e.g., neurons with response fields that barely overlap the choice targets or RDM). Some neurons outside these groups might reflect normalization signals from the T_{in} and M_{in} neurons (***Shushruth et al., 2018***; ***Carandini and Heeger, 2012***).

The fact that the raw averages from a small number of weakly correlated T_{in} neurons furnish a DV on par with that furnished by the full population underscores the importance of this functional class. The role of the M_{in} neurons is less well understood. Freedman and colleagues described direction selective neurons in LIP, similar to our M_{in} neurons (***Freedman and Assad, 2011***; ***Fanini and Assad, 2009***; ***Sarma et al., 2016***). They showed that the neurons represent both the direction of motion and the decision in their task. In contrast, we do not observe the evolution of the decision (*i.e.*, DV) by the M_{in} neurons (Fig. 6). The latency of the direction and coherence-dependent signal as well as its dynamics resemble properties of DS neurons in area MT. We present correlational evidence that the difference between the firing rates of $\mathrm{M}_{\mathrm{in}}^{\mathrm{left}}$ and $\mathrm{M}_{\mathrm{in}}^{\mathrm{right}}$ supplies the momentary evidence that is

integrated by the T_{in}^{con} neurons to produce the drift-diffusion DV. The correlation suggests that the integration of momentary evidence could occur within LIP (***Zhang et al., 2022***). Direct, causal support will require perturbations of functionally identified M_{in} neurons, which is not yet feasible. A natural question is why LIP would contain a copy of the DS signals that are already present in area MT. We suspect it simplifies the routing of momentary evidence from neurons in MT/MST to the appropriate T_{in} neurons. This interpretation leads to the prediction that DS M_{in} neurons would be absent in LIP of monkeys that are naïve to saccadic decisions informed by random dot motion, as has been observed in the SC (***Horwitz et al., 2004***). Further, when motion is not the feature that informs the saccadic response—for example in a color categorization task (*e.g.* ***Kang et al., 2021***)—LIP might contain a representation of momentary evidence for color (***Toth and Assad, 2002***; ***Sereno and Maunsell, 1998***).

The capacity to record from many neurons simultaneously invites characterization of the population in neuronal state space (NSS), in which the activity of each neuron defines a dimension. Often, population activity is confined to a low-dimensional subspace or manifold within the NSS (***Vyas et al., 2020***). An ever-more-popular viewpoint is that representations within these subspaces are emergent properties of the population, rather than *directly* signaled by single neurons, a dichotomy that has its roots in Barlow's neuron doctrine (***Barlow, 1994***). Indeed, it is tempting to conclude that the drift-diffusion signal in LIP is similarly emergent based on our NSS analyses—the identified subspaces (i.e., coding directions) combine neurons with highly diverse activity profiles. In contrast, grouping neurons by the location of their spatial response field reveals a direct coding scheme: T_{in} neurons directly represent the accumulated evidence for making a particular saccade and M_{in} neurons provide the momentary evidence. We argue that this explanation is more parsimonious and, importantly, more principled. Grouping neurons based on spatial selectivity rests on the principle that neurons with similar RFs have similar projections, which is the basis for topographic maps in the visual and oculomotor systems (***Schall, 1995***; ***Silver and Kastner, 2009***; ***Kremkow et al., 2016***; ***Felleman and Van Essen, 1991***). In contrast, there are no principles that guide the grouping of neurons in state space analyses, as the idea is that they may comprise as many dimensions as there are neurons that happen to be sampled by the recording device.

The present finding invites both hope and caution. It may be useful to consider a counterfactual state of the scientific literature that lacks knowledge of the properties of LIP T_{in} neurons—a world without ***Gnadt and Andersen (1988)*** and no knowledge of LIP neurons with spatially selective persistent activity. In this world we have no reason to entertain the hypothesis that decisions would involve neurons that represent the choice targets. We do know about DS neurons in area MT and their causal role in decisions about the direction of random dot motion (***Salzman et al., 1992***; ***Fetsch et al., 2018***; ***Ditterich et al., 2003***; ***Liu and Pack, 2017***). We also know that drift-diffusion models explain the choice-response time behavior. Guided by no particular hypothesis, we obtain population neural recordings in the random dot motion task. We do not perform the saccade and passive viewing control experiments. What might we learn from a data set like ours? We might apply PCA and/or train a choice decoder or possibly a *When*-decoder. If so, we could discover the drift-diffusion signal and we might also infer that the dimensionality of the signal is low. However, we would not discover the T_{in} neurons without a hypothesis and a test. We might notice that the coding directions that reveal drift-diffusion often render a response at the onset of the choice targets as well as increased activity at the time of saccades to the contralateral choice target. These facts might lead us to hypothesize that the population might contain neurons with visual receptive fields and some relationship to saccadic eye movements. We might then query individual neurons, *post hoc*, for these features, and ask if they render the drift-diffusion signal too. The inferences could then be tested experimentally by including simple delayed saccades in the next experiment. The hope in this counterfactual is that data-driven, hypothesis-free methods can inspire hypotheses about the mechanism. The caution is to avoid the natural tendency to stop before the hypotheses and tests, thus accepting as an endpoint the characterization of population dynamics in high dimensions or a lower dimensional manifold. If LIP is representative, these mathematically accurate characterizations may fail to illuminate the neurobiological parsimony.

Methods

Ethical approval declarations. Two adult male rhesus monkeys (*Macacca mulatta*) were used in the experiments. All training, surgery, and experimental procedures complied with guidelines from the National Institutes of Health and were approved by the Institutional Animal Care and Use Committee at Columbia University. A head post and two recording chambers were implanted under general anaesthesia using sterile surgical procedures (for additional details see ***So and Shadlen, 2022***). One recording chamber allowed access to area LIP in the right hemisphere. The other was placed on the midline, allowing access to the superior colliculus. Those recordings are described in ***Stine et al.*** (***2023***). Here we report only on the neural recordings from LIP, focusing on the epoch of decision formation.

Behavioral tasks. The monkeys were trained to interact with visual stimuli presented on a CRT video monitor (Vision Master 1451, Iiyama; viewing distance 57 cm; frame rate 75 Hz). They were trained to control their gaze and make saccadic eye movements to peripheral targets to receive a liquid reward (juice). The direction of gaze was monitored by an infrared camera (EyeLink 1000; SR Research, Ottawa, Canada; 1 kHz sampling rate). The tasks involve stages separated by random delays, distributed as truncated exponential distributions

$$f(t) = \begin{cases} \frac{\alpha}{\lambda} e^{-\frac{t-t_{min}}{\lambda}} & t_{\min} \leq t \leq t_{\max} \\ 0 & \text{otherwise} \end{cases} \tag{1}$$

where $t_{\min}$ and $t_{\max}$ define the range, λ is the time constant, and α is chosen to ensure the total probability is unity. Below, we provide the range ($t_{\min}$ to $t_{\max}$) and the exponential parameter λ for all variable delays. Note that because of truncation, the expectation $\mathbb{E}(t) < t_{\min} + \lambda$.

In the *main task* (Fig. 1a) the monkey must decide the net direction of random dot motion and indicate its decision when ready by making a saccadic eye movement to the corresponding choice target. After acquiring a central fixation point (FP) and a random delay (0.25–0.7 s, λ =0.15), two red choice-targets (diameter 1 dva) appear in the left and right visual fields. The random dot motion is then displayed after a random delay (0.25 – 0.7 s, λ =0.4 s) and continues until the monkey breaks fixation. The dots are confined to a circular aperture (diameter 5 dva; degrees visual angle) centered on the fixation point (dot density 16.7 dots·dva^{-2}·s^{-1}). The direction and strength of motion are determined pseudorandomly from $\pm\{0, 3.2, 6.4, 12.6, 25.6, 51.2\}$% coherence (coh). The sign of the coh indicates direction (positive for leftward; i.e., contraversive with respect to the neural recording site). The values control the probability that a dot plotted on frame n will be displaced by Δx on frame $n + 3$ (Δt =40 ms), as opposed to randomly replaced, where $\Delta x = \frac{5}{75}$ dva, consistent with 5 dva·s^{-1} speed of apparent motion (***Roitman and Shadlen, 2002***, see also). The monkey is rewarded for making a saccadic eye movement to the appropriate choice target. On trials with 0% coh motion, either saccadic choice is rewarded with probability $\frac{1}{2}$. Errors are punished by extending the intertrial interval by up to 3 s (see ***Stine et al., 2022***, for additional details). On approximately half of the trials, a 100 ms pulse of weak motion ($\pm$4% coh) is added to the random dot motion stimulus at a random time (0.1–0.8 s, λ =0.4) relative to motion onset (similar to ***Kiani et al., 2008***). Monkey M performed 9684 trials (5 sessions); monkey J performed 8142 trials (3 sessions). The data are also analyzed in a companion paper that focuses on the termination of the decision (***Stine et al., 2022***, ***2023***).

In the *visually instructed delayed saccade task* (***Hikosaka and Wurtz, 1983***), one target is displayed at a pseudo-random location in the visual field. After a variable delay (monkey M: 0.4–1.1 s, λ =0.3; monkey J: 0.5–1.5 s, λ =0.2) the fixation point is extinguished, signalling 'go'. The monkey is rewarded for making a saccade to within $\pm$2.5 dva of the location of the target. In a *memory-guided* variant of the task (***Gnadt and Andersen, 1988***), the target is flashed briefly (200 ms) and the monkey is required to make a saccade to the remembered target location when the fixation point is extinguished. These tasks provide a rough characterization of the neural response fields during the visual, perisaccadic and delay epochs. Neurons are designated $\mathrm{T}_{\mathrm{in}}^{\mathrm{con}}$ if they exhibit spatially selective activity at the location of the response target in the visual hemifield contralateral to the recorded hemisphere. This determination is made before analyzing the activity in the random dot motion task. We refer to the unweighted mean firing rate as $S_{\mathrm{Tin}}^{\mathrm{con}}$. Neurons are designated $\mathrm{T}_{\mathrm{in}}^{\mathrm{ips}}$ if they exhibit spatially selective activity at the location of

the response target in the visual hemifield ipsilateral to the recorded hemisphere. These analyses were conducted *post hoc*, after spike sorting.

The *passive motion-viewing task* is identical to the main task, except there are no choice targets and only the strongest motion strength (±51.2% coherence) is displayed for 500 ms (1 s on a small fraction of trials in session 1). The direction is left or right, determined randomly on each trial ($P_{\text{left}} = \frac{1}{2}$). The monkey is rewarded for maintaining fixation until the random dot motion is extinguished.

Behavioral analyses. We fit a variant of the drift-diffusion model (Fig. 1c) to the choice-RT data from each session. Details of the model and the fitting method are described in ***van Den Berg et al.*** (***2016***). The model constructs the decision process as a race between two accumulators: one accumulating evidence for left and against right (*e.g.*, left minus right) and one accumulating evidence for right and against left (*e.g.*, right minus left). The decision is determined by the accumulator that first exceeds its positive decision bound, at which point the decision is terminated. The races are negatively correlated with one another, owing to the common source of noisy evidence. We assume they share half the variance, $\rho = -\sqrt{0.5} \approx -0.71$, but the results are robust to a wide range of reasonable values. The decision bounds are allowed to collapse linearly as a function of time, such that

$$B(t) = B_0 - \alpha t, \quad \alpha \geq 0 \tag{2}$$

We used the method of images to compute the probability density of the accumulated evidence for each accumulator (which both start at zero at $t = 0$) as a function of time (t) using a time-step of 1 ms. The decision time distributions rendered by the model were convolved with a Gaussian distribution of the non-decision times, t_{nd}, which combines sensory and motor delays, to generate the predicted RT distributions. The model has six parameters: κ, B_0, α, μ_{nd}, σ_{nd}, and C_0, where κ determines the scaling of motion strength to drift rate, C_0 implements bias in units of signed coherence (***Hanks et al., 2011***), μ_{nd} is the mean non-decision time and σ_{nd} is its standard deviation.

Neurophysiology. We used prototype "alpha" version Neuropixels1.0-NHP45 probes (IMEC/HHMI-Janelia) to record the activity of multiple isolated single-units from the ventral subdivision of area LIP (LIP_v; ***Lewis and Van Essen 2000***). We used anatomical MRI to identify LIP_v and confirmed its physiological hallmarks with single-neuron recordings (Thomas Recording GmbH) before proceeding to multi-neuron recordings. Neuropixels probes enable recording from 384 out of 4416 total electrical contacts distributed along the 45 mm long shank. All data presented here were recorded using the 384 contacts closest to the tip of the probe (Bank 0), spanning 3.84 mm. Reference and ground signals were directly connected to each other and to the monkey's head post. A total of 1084 neurons were recorded over eight sessions (54–203 neurons per session). (Table 1).

Session	1	2	3	4	5	6	7	8	mean
monkey	M	M	M	M	M	J	J	J	
trials	1797	1696	2256	1859	2076	2449	2799	2894	2228
neurons	191	90	54	140	107	138	161	203	135.5
% $\text{T}_{\text{in}}^{\text{con}}$	8.9	14.4	16.7	15	17.8	8.7	21.1	13.3	14.5
% $\text{T}_{\text{in}}^{\text{ips}}$	4.2	5.6	13	13.6	6.5	12.3	0.6	2.0	7.2
% $\text{M}_{\text{in}}^{\text{left}}$	5.2	5.6	0	5	3.7	2.9	3.7	7.4	4.2
% $\text{M}_{\text{in}}^{\text{right}}$	1.0	2.2	3.7	1.4	2.8	3.6	2.5	3.0	2.5

Table 1. Information about individual experimental sessions.

The Neuropixels 1.0-NHP45 probe uses a standard Neuropixels 1.0 headstage and is connected via the standard Neuropixels1.0 5m cable to the PCI eXtensions for Instrumentation (PXIe) hardware (PXIe-1071 chassis and PXI-6141 and PXIe-8381 I/O modules, National Instruments). Raw data were acquired using the SpikeGLX software

(http://billkarsh.github.io/SpikeGLX/), and single-units were identified offline using the Kilosort 2.0 algorithm (***Pachitariu et al., 2016***; ***Pachitariu, 2021***), followed by manual curation using Phy (https://github.com/cortex-lab/phy). The spike times were then synchronized with task events acquired by the experimental control system (Rex, ***Hays et al. 1982***; OmniPlex, Plexon Inc.).

Neural data analysis. The spike times from each neuron are represented as delta functions of discrete time, $s_{i,n}(t)$ on each trial i and each neuron n ($dt = 1$ ms). The weighted sum of these $s_{i,n}(t)$ give rise to the single trial population signals:

$$S_i^x(t) = \sum_n w_n s_{i,n}(t) \tag{3}$$

where the superscript, x, identifies the method used to establish weights. For visualization, the single-trial signals are smoothed by convolution with a truncated Gaussian using the Matlab function, *gausswin* (width = 80 ms, width-factor = 1.5, $\sigma \approx 26$ ms). Unless otherwise specified, for all other analyses, we use a 50 ms boxcar (rectangular) filter.

We used several methods to define coding directions in the neuronal state space defined by the population of neurons in each session. For PCA and choice-decoding, we standardized the single trial firing rates for each neuron using the mean and standard deviation of its firing rate at $75 \leq t \leq 125$ ms after motion onset. In some sessions, this led to the exclusion of a small number of neurons with very low firing rates that did not produce any spikes in the normalization window (*i.e.*, 75–125 ms after motion onset). Those neurons (5 in session 1 and no more than 2 in other sessions) were assigned zero weight.

Ramp direction. We applied regression to best approximate a linear ramp, on each trial, i, that terminates with a saccade to the choice-target contralateral to the hemisphere of the LIP recordings. The ramps are defined on the epoch spanning the decision time: from $t_0 = 0.2$ s after motion onset to $t_1 = t_{\text{sac}} - 0.1$ s (*i.e.*, 100 ms before saccade initiation). Each ramp begins at $f_i(t_0) = -1$ and ends at $f_i(t_1) = 1$ (see Fig. S4). The dependent variables of the regression model (neural activities) were z-scored. We employed a lasso linear regression with $\lambda = 0.005$. The vector of weights assigned across the neurons defines a direction in neuronal state space, S^{ramp}, which we use to render the signal $S^{\text{ramp}}(t)$ on single trials by projecting the data onto this direction. To determine the effect of the regularization term in the lasso regression, we recomputed single-trial signals using standard linear regression (without regularization). We then calculated the Pearson correlation between single-trial traces generated by projecting neural data onto the two alternative encoding directions (with and without regularization) were strongly correlated. Within-trial correlations of $r = 0.99$ (mean across sessions) indicate that results are robust to changes in the degree of regularization applied. Here and elsewhere we compute the mean r using the Fisher-z transform, such that

$$\bar{r} = Z^{\text{inv}}\left(\mathbb{E}\left[Z(r_k)\right]\right) \tag{4}$$

where Z^{inv} is the inverse Fisher-z.

Principal Components Analysis (PCA). We applied standard PCA to the firing rate averages for each neuron using all trials sharing the same signed motion coherence in the shorter of two epochs: 200 ms to either 600 ms after motion onset or 100 ms before the median RT for the signed coherence, whichever produces the shorter interval. As in all other analyses of neural activity aligned to motion onset, we exclude data in the 100 ms epoch ending at saccade initiation on each trial. We projected the neural data onto the first PC to generate the signal S^{PC1}.

Choice decoder. For each experimental session, we trained logistic choice decoders with lasso regularization ($\lambda = 0.01$) on the population activity in 50 ms time bins spanning the first 500 ms after motion onset and spanning the 300 ms epoch ending at saccade initiation. Each of the decoders was trained on the even-numbered trials. Decoder accuracy was cross-validated using the activity of held-out trials at the same time point (Fig. 4a). For the time bins beginning at motion onset, we also assessed the accuracy of the decoders trained on each of the time bins to predict the choice on time bins on which they were not trained (Fig. 4b)(***King and Dehaene, 2014***). We use the decoder trained on the bin centered on $t = 450$ ms to define the *What* coding direction.

We applied a similar analysis to simulated data. We fit the race model described above to the combined behavioral

data across all sessions and used the best-fitting parameters to simulate 60,000 trials of the motion discrimination task. Each simulated trial yields a time series for two decision variables, one for each accumulator in the race. We assume that the model-derived non-decision time ($t_{\mathrm{nd}} = 307$ ms; Fig. 1b) comprises delays at both the beginning and end of the decision: 200 ms from motion onset to the beginning of evidence integration and the remaining 107 ms after termination. We simulated the latter delay using a Normal distribution, $\mathcal{N}(\mu, \sigma)$, where $\mu = 107$ ms and $\sigma = 50$ ms. The latter approximates the variability observed in the saccadic latencies in the delayed saccade task (***Stine et al., 2023***). In the variable post-termination delay (ending in the saccade), the simulated DVs were assigned the values they had attained at the start of the delay. We then applied the logistic decoder described above to the decision variable associated with a contralateral choice to generate the black curve in Fig. 4a. Assuming a stochastic drift-diffusion process giving rise to choice and response times, the exercise produces rough upper bound on decoder accuracy, were the actual drift-diffusion process were known precisely.

When decoder. This decoder is trained to predict whether a saccade to the left (contalateral) choice target will occur within the next 150 ms. We applied logistic regression with lasso regularization ($\lambda = 0.01$) to spike counts from each neuron in discrete bins of 25 ms, from 200 ms before motion onset to 50 ms before the saccade. We used only trials ending in a left choice and trained the decoder on the even numbered half of those trials. The concatenation of these trials forms a sequence of step functions which are set to 1 if a saccade occurred within 150 ms of the start of the 25 ms time bin and 0 otherwise (Fig. S7).

The spike counts were also concatenated across these trials to construct column vectors (one per neuron) that match the vector of concatenated step functions. These concatenated vectors, one per neuron, plus an offset (β_0), serve as the independent variables of the regression model (one β term per neuron). The proportion of β weights equal to zero—controlled by the lasso parameter, λ—was 0.8 ± 0.02 (across sessions). The weights define the S^{When} coding direction, which yields single-trial signals, $S^{\mathrm{When}}(t)$. The When-decoder signal is $S^{\mathrm{When}}(t) + \beta_0$. We validated the When-decoder by computing the area under an ROC (AUC) using the held-out (odd-numbered) trials ending in left choices (mean AUC over all time points and sessions: 0.84).

Our motivation, however, was to ascertain whether the *When* coding direction would predict the monkey's choices on *all trials*—that is, to perform as a *What* decoder.
To this end, we predicted the choice using the sign of the detrended $S^{\mathrm{When}}(t)$, formed by subtracting the average of the signal using all trials:

$$S_i^*(t) = S_i^{\mathrm{When}}(t) - \langle S_i^{\mathrm{When}}(t) \rangle_i \tag{5}$$

where $\langle \cdots \rangle_i$ denotes expectation across all trials contributing values at time t. The choice accuracy is

$$A_i(t) = \begin{cases} 1 & S_i^*(t) > 0 \ \& \ \mathrm{choice}_i = \mathrm{left} \\ 1 & S_i^*(t) \leq 0 \ \& \ \mathrm{choice}_i = \mathrm{right} \\ 0 & \mathrm{otherwise} \end{cases}$$

The green trace in Fig. 4a shows $\langle A_i(t) \rangle_i$.

Leverage of single-trial activity on behavior. The leverage of single-trial signals, $S^x(t)$, on choice and RT was assessed using the earliest 300 ms epoch of putative integration ($0.2 < t < 0.5$ s from motion onset), restricting analyses to trials with RTs outside this range ($0.67 < \mathrm{RT} < 2$ s). The single-trial signals are smoothed with a 50 ms boxcar filter and detrended by subtracting the mean $S(t)$ for trials sharing the same motion strength and direction (*i.e.*, signed coherence). The reaction times were also expressed as residuals relative to the mean RT from trials sharing the same signed coherence and choice. We include trials with $|\mathrm{coh}| \leq 0.064$ that result in choices of the left response target in this analysis. The leverage on RT is the Pearson correlation between the residual signals $\tilde{S}(t)$ at each time $0.2 < t \leq 0.5$, and $\tilde{\mathrm{RT}}$ on that trial, where the tilde indicates residual. Correlations were computed per session and then averaged across sessions (Eq. 4). We also show the correlation at t=0.55 s, using the ordered pairs, $\{\tilde{S}(t = 0.55), \tilde{\mathrm{RT}}\}$ and we assess the mediation of this later sample of S^x on the earlier samples by computing partial correlations $\{\tilde{S}(t), \tilde{\mathrm{RT}} \mid \tilde{S}(t = 0.55)\}$, also notated $R_{\tilde{S}(t),\tilde{RT}|\tilde{S}(0.55)}$ in (Fig. 5). We show this mediation at all time points. We also report a mediation statistic (ξ^{RT}) using the time point 200 ms after the

beginning of putative integration (i.e., $S(t = 0.4)$):

$$\xi^{\mathrm{RT}} = 1 - \frac{R^2_{\tilde{S}(0.4),\tilde{\mathrm{RT}}\,|\,\tilde{S}(0.55)}}{R^2_{\tilde{S}(0.4),\tilde{\mathrm{RT}}}} \tag{6}$$

Fits in which there was no negative correlation between $S(t = 0.4)$ and RT were excluded from this summary statistic, for in this case no mediation is possible. The rationale for using this time point is *(i)* to allow the process to have achieved enough leverage on RT so that a reduction is meaningful and (*ii*) to preserve a substantial gap between this time and the sample at $t = 0.55$ s (e.g., to avoid autocorrelations imposed by smoothing). When combining values of ξ^{RT} across sessions, we rectify any $R_{\tilde{S}(t),\tilde{RT}|\tilde{S}(0.55)} > 0$ to 0. This occurs rarely when the mediated correlation is near zero, typically at early times.

We compute the leverage on choice, ξ^{Ch}, using trials with $|\mathrm{coh}| \leq 0.064$ and the same time points as for ξ^{RT}. Instead of an R-squared measure, we based ξ^{Ch} on coefficients derived from logistic regression:

$$P^{\mathrm{con}}(t) = \frac{1}{1 + e^{-\left(\beta_0^{\mathrm{coh}} + \beta_1(t)S(t)\right)}}, \quad 0.2 \leq t \leq 0.5. \tag{7}$$

where β_0^{coh} is a set of constants that accounts for the proportion of contralateral choices at each signed motion strength and $\beta_1(t)$ is the simple leverage of S(t) on choice, analogous to simple correlation. The regression analysis was performed separately for each session. The coefficients $\beta_1(t)$ were divided by their standard error and then averaged across sessions. This normalization step was implemented to control for potential variation in the magnitude of $S(t)$ (and therefore of $\beta_1(t)$) across sessions. Analogous to partial correlation, we include the later time point and fit

$$P^{\mathrm{con}}(t) = \frac{1}{1 + e^{-\left(\beta_0^{\mathrm{coh}} + \beta_1^*(t)S(t) + \beta_2 S(0.55)\right)}} \tag{8}$$

where $\beta_1^*(t)$ is the amount of leverage at time t given the $S(0.55)$. The regression coefficients $\beta_1^*(t)$ were averaged across sessions after dividing them by the standard error of the $\beta_1(t)$ coefficients obtained from 7. That is, the same normalization factors were used for the mediated and unmediated leverage. The summary statistic for choice mediation is defined by

$$\xi^{\mathrm{Ch}}(t) = \begin{cases} 1 & \beta_1^*(t) \leq 0 \\ 1 - \frac{\beta_1^*(t)}{\beta_1(t)} & \beta_1^*(t) > 0 \\ \text{undefined} & \beta_1(t) \leq 0 \text{ (\textit{i.e.}, mediation is not possible)} \end{cases} \tag{9}$$

For both types of mediation, we also test whether the earlier $S(t)$ is mediated by the $\mathrm{T_{in}}$ neurons by substituting $S_{\mathrm{Tin}}(0.55)$ for $S(0.55)$ in Eq. 8 and in the expression for partial correlations.

Similarity of single-trial signals, $S^x(t)$. We used Pearson correlation to quantify the similarity of the stochastic (diffusion) signals generated by diverse coding directions. For each trial, k, we use the detrended signals, $\tilde{S}^x_k$ and $\tilde{S}^y_k$, to obtain ordered pairs, $\{\tilde{S}^x(t_i), \tilde{S}^y(t_i)\}$ using times from $t_1 = 0.2$ s to $t_{\mathrm{end}} = t_{\mathrm{sac}} - 0.1$ s. Each trial gives rise to a correlation coefficient, r_k. We report the mean r using the Fisher-z transform using Eq. 4. As above, detrending removes the mean response of trials sharing the same signed motion coherence. The ordered pairs $\{\tilde{S}^x(t_i), \tilde{S}^y(t_i)\}$ r-values for comparisons across all signals are summarized in Fig. S8f.

Noise correlation between neurons. The mean pairwise correlation between $\mathrm{T}^{\mathrm{con}}_{\mathrm{in}}$ neurons, reported in Results, is based on all pairs of simultaneously recorded $\mathrm{T}^{\mathrm{con}}_{\mathrm{in}}$ neurons in each session and all trials with RT > 0.5 s. For each neuron and each trial, we compute the time-averaged $S^{\mathrm{con}}_{\mathrm{Tin}}(t)$ over the epoch $0.2 \leq t \leq 0.4$. These scalar values are converted to residuals by subtracting the mean (for each neuron) across all trials sharing the same signed motion coherence and compute $N \times (N - 1)$ Pearson r values, where N is the number of $\mathrm{T}^{\mathrm{con}}_{\mathrm{in}}$ neurons in the session. The mean correlations for all pairs of $\mathrm{T}^{\mathrm{con}}_{\mathrm{in}}$ neurons and across all sessions is computed using Eq. 4. The reported mean

is significantly greater than the mean pairwise correlation between all pairs, excluding T_{in}^{con} neurons (0.01 ± 0.0003; $t(81277) = 28.1$; $p < 10^{-172}$).

Direction selective neurons. We identified direction-selective (DS) neurons (M_{in} neurons) using the passive motion-viewing task (described above).To classify a neuron as M_{in}, we required (1) a short latency response to the onset of random dot motion followed by (2) a direction-selective response favoring leftward or rightward motion. Neurons that satisfy the first criterion typically exhibited either a large (5-fold) increase in firing rate in the *immediate post-onset* epoch ($0 < t \leq 0.08$ s) compared to *baseline* ($-0.2 \leq t \leq 0$ s), where $t = 0$ at motion onset. We also include neurons with weaker responses if simple least squares regression of the mean firing rate showed a larger positive slope in the *immediate post-onset* epoch compared to the *baseline* epoch. To satisfy the second criterion, we compared the distribution of firing rates to leftward and rightward motion and required the area under an ROC (AUC) to exceed 0.6 in at least one of two epochs: *early* ($0.15 \leq t < 0.3$ s) or *late* ($t \geq 0.3$s). We excluded one neuron that changed direction preference in the two epochs.

Latency analysis. We estimated the latency of direction-selective responses using the CUSUM method (***Ellaway, 1978***; ***Lorteije et al., 2015***). We employed a receiver operating characteristic (ROC) analysis to estimate the selectivity of each M_{in} neuron to motion direction. The AUC reflects the separation of the distributions of spike counts (100 to 400 ms after motion onset) on single trials of leftward and rightward motion, respectively. We only included correct trials with response times greater than 450 ms and motion strengths above 10% coherence. For each neuron with AUC > 0.6, we computed the difference in spike counts (25 ms bins) between trials featuring leftward and rightward motion. Subsequently, we accumulated these differences over time, following the CUSUM method. The resulting difference is approximately zero before the onset of direction selectivity and then either increases or decreases monotonically, depending on the preferred motion direction. To identify the transition between these two regimes, we fit a dog leg function to the cumulative sum of spikes: a flat line starting at $t_0 = 0$ followed by a linearly increasing component beginning at $t_1 > t_0$. The time of the end of the flat portion (between 0 and 500 ms from motion onset) of the fit was taken as the latency. Estimating latencies based on cumulative sums of spikes helps mitigate the effect of neuronal noise. The fitting step reduces the effect of the number of trials on latency estimates (*e.g.*, based on traditional methods that rely on t-tests in moving windows).

Correlations between M_{in} and T_{in}^{con}. The analysis of the correlations shown in Fig. 6d is based on the spike counts of the M_{in}^{left}, M_{in}^{right}, and T_{in}^{con} neurons calculated in 25 ms windows. We computed residuals by subtracting from each trial and time bin its average over trials of the same signed coherence. The spike count residuals were then z-scored independently for each time bin and session. Trials from different sessions were concatenated, and the baseline activity—last 100 ms before motion onset—was subtracted from each trial. We refer to the resulting signals as $\tilde{S}_{Min}^{left}$, $\tilde{S}_{Min}^{right}$, and $\tilde{S}_{Tin}^{con}$. Trials with response time less than 0.55 s were discarded, and the correlations between the difference, $\tilde{S}_{Min}^{left} - \tilde{S}_{Min}^{right}$, and $\tilde{S}_{Tin}^{con}$ were calculated for all pairs of time steps between 0 and 500 milliseconds (Fig. 6d). Statistical significance was assessed using permutation tests. Two regions of interest (ROI) were defined based on the time from stimulus onset for the M_{in} (x) and T_{in} (y) dimensions. The first region of interest, ROI_1, is characterized by $t_x > 100$, $t_y > 200$, and $t_y > t_x$. According to our hypothesis of a causal influence of M_{in} on T_{in}, we anticipated high correlations in this region. The second region of interest, ROI_2, is defined by $t_x > 100$, $t_y > 200$, and $t_y < t_x$. If, contrary to our hypothesis, M_{in} had a causal influence on T_{in}, we would expect high correlations in this region. We calculated the difference in correlations between these two groups, $\langle \rho_{ROI1} \rangle - \langle \rho_{ROI2} \rangle$, where the expectation is over the time bins within each region of interest. This difference was compared to those obtained after randomly shuffling the order of the trials for one of the dimensions before calculating the pairwise correlations ($N_{shuffles} = 200$). We fit the differences obtained from the shuffled data to a normal distribution and evaluated the significance as the probability of obtaining a value as extreme as the one observed in the experimental data. The analysis was repeated with an alternative ROI_2 defined by $t_x < 100$ and $t_y < 200$, representing the times before direction selectivity is present in at least one of the two dimensions.

Correlations between M_{in} signals and behavior. To assess the leverage of M_{in} signals on choice and RT (Fig. 6e & f, respectively) we performed the same logistic regression and pairwise correlation analyses as in Fig. 5, substituting

the M_{in}^{left} and M_{in}^{right} for S^x. The leverage on choice is not mediated by a later sample of either M_{in} signal ($\xi^{Ch} \leq$ 9.6%; not shown), and there is negligible leverage on RT to mediate. We suspect the failure to detect leverage of M_{in} is explained by a lack of power, owing to the focus on long RT trials, narrow sample windows (50 ms boxcar), and the small number of M_{in}^{left} and M_{in}^{right} neurons. We support this assertion with a simpler correlation analysis, using the difference of the M_{in} signals (standardized as in the previous paragraph):

$$\psi_k = \text{mean}\left(\tilde{S}_{\text{Min}}^{\text{left}}(t) - \tilde{S}_{\text{Min}}^{\text{right}}(t)\right)$$

on the interval $0.1 \leq t \leq 0.4$ s from motion onset, on each trial, k, including trials with contraversive choices and RT $\geq$ 500 ms. We calculated the Pearson correlation coefficient between ψ_k and RT. Response times were z-scored independently for each signed motion strength and session. We evaluated the null hypothesis that the correlation coefficient was non-negative. The reported p-value is based on t-statistic.

Auto-covariance of smoothed diffusion signals. The analyses in Fig. 3 compare variance and autocovariance measure in the single-trial signals to unbounded drift-diffusion. To mitigate the effect of the bound, we therefore restrict the epoch to the earliest epoch of putative integration (200 to 531 ms after motion onset) and weakest motion strengths ($|\text{coh}| \leq 3.2\%$). The variance as a function of time and the autocovariance as a function of time and lag are well known for the cumulative sum of discrete *iid* random samples, but the autocovariance is affected by the boxcar filter we applied to render the signals. We incorporated the correction in our characterization of unbounded diffusion. The derivation is summarized in Appendix 1, and we provide Matlab code in the GitHub repository. The theoretical values shown in Fig. 3 assume a 1 kHz sampling rate and standard Wiener process (i.e., samples drawn from a normal distribution with $\{\mu = 0, \sigma = \sqrt{dt}\}$. The evolution of variance would be a line from 0 to 1 over the first second of integration. The key prediction, shown in Fig. 3a is that the variance at the first measure should achieve twice that value at the next step (same Δt). We therefore use arbitrary units normalized to the measured variance of the first point. We do not know the variance of the drift-diffusion signal that $S(t)$ is thought to approximate, but we assume it can be decomposed—by the law of total variance—to a component given by drift-diffusion and components associated with spiking and other nuisance factors. We therefore search for a scalar non-negative factor $\phi \leq 1$ that multiplies all terms in the diagonal of the empirical covariance matrix (*i.e.*, the variance) before normalizing to produce the autocorrelation matrix. We search for the value of ϕ that minimizes the sum of squares between Fisher-z transformed correlation coefficients in the theoretical and empirical autocorrelation matrices (Fig. 3.

Appendix

We consider a discrete time (sampling interval dt) Wiener process with independent random increments ϵ_k on time step k that are zero-mean noise with variance $\sigma^2(\epsilon_k) = dt$ (i.e. unit variance per second). The accumulated evidence (i.e. decision variable, DV) on time step p is

$$DV_p = \sum_{k=1}^{p} \epsilon_k \tag{10}$$

For such a Wiener process,

$$\text{Cov}(DV_p, DV_q) = \text{Cov}\left(\sum_{j=1}^{p} \epsilon_j, \sum_{k=1}^{q} \epsilon_k\right) = \sum_{j=1}^{p}\sum_{k=1}^{q} \text{Cov}(\epsilon_j, \epsilon_k)$$

As the increments ϵ_k are independent across time, $\text{Cov}(\epsilon_j, \epsilon_k)$ is 0 for $j \neq k$ and dt for $j = k$

$$\mathrm{Cov}(DV_p, DV_q) = \sum_{j=1}^{\min(p,q)} \mathrm{Cov}(\epsilon_j, \epsilon_j) = \min(p,q)dt.$$

We define the mean DV over a window of $\pm n$ points as

$$MDV_p^n = \frac{1}{2n+1} \sum_{j=-n}^{n} DV_{p+j} \tag{11}$$

We consider two time points $p < q$ with window n such that there is no overlap and hence $p + n < q - n$

$$\begin{aligned}
\mathrm{Cov}(MDV_p^n, MDV_q^n) &= \mathrm{Cov}\left(\frac{1}{2n+1}\sum_{j=-n}^{n} DV_{p+j}, \frac{1}{2n+1}\sum_{k=-n}^{n} DV_{q+k}\right) \\
&= \frac{1}{(2n+1)^2}\sum_{j=-n}^{n}\sum_{k=-n}^{n} \mathrm{Cov}(DV_{p+j}, DV_{q+k}) \\
&= \frac{dt}{(2n+1)^2}\sum_{j=-n}^{n}\sum_{k=-n}^{n} \min(p+j, q+k) \\
&= \frac{dt}{(2n+1)^2}\sum_{j=-n}^{n}\sum_{k=-n}^{n} p+j \\
&= \frac{dt}{(2n+1)^2}(2n+1)^2 p = p.dt
\end{aligned}$$

$$\begin{aligned}
\mathrm{Var}(MDV_p^n) &= \mathrm{Var}\left(\frac{1}{2n+1}\sum_{j=-n}^{n} DV_{p+j}\right) \\
&= \frac{1}{(2n+1)^2}\sum_{j=-n}^{n}\sum_{k=-n}^{n} \mathrm{Cov}(DV_{p+j}, DV_{p+k}) \\
&= \frac{1}{(2n+1)^2}\sum_{j=1}^{2n+1}\sum_{k=1}^{2n+1} \mathrm{Cov}(DV_{p-n-1+j}, DV_{p-n-1+k}) \\
&= \frac{dt}{(2n+1)^2}\sum_{j=1}^{2n+1}\sum_{k=1}^{2n+1} \min(p-n-1+j, p-n-1+k) \\
&= \frac{dt}{(2n+1)^2}\left[(2n+1)^2(p-n-1) + \sum_{j=1}^{2n+1}\sum_{k=1}^{2n+1} \min(j,k)\right]
\end{aligned}$$

Given that $\sum_{j=1}^{n}\sum_{k=1}^{n} \min(j,k) = \sum_{j=1}^{n} j^2 = n(n+1)(2n+1)/6$

$$\begin{aligned}
\mathrm{Var}(MDV_p^n) &= \frac{dt}{(2n+1)^2}[(2n+1)^2(p-n-1) + (2n+1)(2n+2)(4n+3)/6] \\
&= \frac{3p + 6np - 2n - 2n^2}{3(2n+1)} dt
\end{aligned}$$

Therefore the correlation

$$\begin{aligned}\mathrm{Corr}(MDV_p^n, MDV_q^n) &= \frac{\mathrm{Cov}(MDV_p^n, MDV_q^n)}{\sqrt{\mathrm{Var}(MDV_p^n)\mathrm{Var}(MDV_q^n)}} \\ &= \frac{3p(2n+1)}{\sqrt{(3p+6np-2n-2n^2)(3q+6nq-2n-2n^2)}}\end{aligned}$$

In contrast for the point estimates at p and q

$$\mathrm{Corr}(DV_p, DV_q) = \sqrt{\frac{p}{q}}$$

It is useful to re-express the above two equations in terms of actual time t_p and t_q and window size t_n. Substituting for p, q, and n with t_p/dt, t_q/dt and t_n/dt

$$\begin{aligned}\mathrm{Corr}(MDV_{t_p}^{t_n}, MDV_{t_q}^{t_n}) &= \frac{3t_p(2t_n+dt)}{\sqrt{(3t_p\,dt+6t_nt_p-2t_n\,dt-2t_n^2)(3t_q\,dt+6t_nt_q-2t_n\,dt-2t_n^2)}} \\ &= \frac{3t_p(2t_n+dt)}{\sqrt{((3t_p-2t_n)dt+6t_nt_p-2t_n^2)((3t_q-2t_n)dt+6t_nt_q-2t_n^2)}}\end{aligned}$$

$$\mathrm{Corr}(DV_{t_p}, DV_{t_q}) = \sqrt{\frac{t_p}{t_q}}$$

Acknowledgments

We thank Shushruth, NaYoung So, and David Gruskin for comments on the manuscript, Cornel Duhaney and Brian Madeira for their assistance in the planning and execution of surgeries, animal training and general support, and we thank Columbia University's ICM for the quality of care they provide for our animals, especially during the pandemic and lockdown. We would further like to thank Tanya Tabachnik and her team at the Zuckerman Institute Advanced Instrumentation Core and Tim Harris, Wei-lung Sun, Jennifer Colonell, and Bill Karsh at HHMI Janelia for their continued support with Neuropixels1.0-NHP45 probes development and testing. This research was supported by the Howard Hughes Medical Institute; an R01 grant from the NIH Brain Initiative (M.N.S., R01NS113113); a T32 and F31 grant from the National Eye Institute (G.M.S, T32 EY013933, F31 EY032791); the Grossman center; and the Brain and Behavior Research Foundation.

Author contributions

G.M.S. and M.N.S. designed the experiment. N.A.S., G.M.S. and E.M.T. implemented the experimental set-up. G.M.S. collected the data. N.A.S., G.M.S., A.Z., D.M.W and M.N.S. analyzed the data. All authors wrote the manuscript.

Data availability statement

Data and code are available upon request.

References

Barlow H. The Neuron Doctrine in Perception. In: Gazzaniga M, editor. *The Cognitive Neurosciences* The Cognitive Neurosciences, Boston: MIT Press; 1994.p. 415–435.

Bollimunta A, Ditterich J. Local computation of decision-relevant net sensory evidence in parietal cortex. Cerebral cortex. 2012; 22(4):903–917.

Britten KH, Newsome WT, Shadlen MN, Celebrini S, Movshon JA. A relationship between behavioral choice and the visual responses of neurons in macaque MT. Visual neuroscience. 1996; 13(1):87–100.

Carandini M, Heeger DJ. Normalization as a canonical neural computation. Nature Reviews Neuroscience. 2012; 13(1):51–62.

Churchland AK, Kiani R, Chaudhuri R, Wang XJ, Pouget A, Shadlen MN. Variance as a signature of neural computations during decision making. Neuron. 2011; 69(4):818–31. https://www.ncbi.nlm.nih.gov/pubmed/21338889, doi: 10.1016/j.neuron.2010.12.037.

Cisek P, Puskas GA, El-Murr S. Decisions in changing conditions: the urgency-gating model. The Journal of neuroscience : the official journal of the Society for Neuroscience. 2009 09; 29(37):11560 – 11571. http://www.jneurosci.org/cgi/content/full/29/37/11560, doi: 10.1523/jneurosci.1844-09.2009.

van Den Berg R, Anandalingam K, Zylberberg A, Kiani R, Shadlen MN, Wolpert DM. A common mechanism underlies changes of mind about decisions and confidence. Elife. 2016; 5:e12192.

Ding L, Gold JI. Neural correlates of perceptual decision making before, during, and after decision commitment in monkey frontal eye field. Cereb Cortex. 2012; 22(5):1052–67. http://www.ncbi.nlm.nih.gov/pubmed/21765183, doi: 10.1093/cercor/bhr178.

Ditterich J, Mazurek ME, Shadlen MN. Microstimulation of visual cortex affects the speed of perceptual decisions. Nature Neuroscience. 2003; 6(8):891 – 898. http://www.nature.com/neuro/journal/v6/n8/abs/nn1094.html, doi: 10.1038/nn1094.

Drugowitsch J, Moreno-Bote R, Churchland AK, Shadlen MN, Pouget A. The Cost of Accumulating Evidence in Perceptual Decision Making. J Neurosci. 2012; 32(11):3612–3628. doi: 10.1523/JNEUROSCI.4010-11.2012.

Ellaway P. Cumulative sum technique and its application to the analysis of peristimulus time histograms. Electroencephalography and clinical neurophysiology. 1978; 45(2):302–304.

Fanini A, Assad JA. Direction selectivity of neurons in the macaque lateral intraparietal area. Journal of neurophysiology. 2009; 101(1):289–305.

Felleman DJ, Van Essen DC. Distributed hierarchical processing in the primate cerebral cortex. Cerebral cortex (New York, NY: 1991). 1991; 1(1):1–47.

Ferraina S, Paré M, Wurtz RH. Comparison of cortico-cortical and cortico-collicular signals for the generation of saccadic eye movements. Journal of neurophysiology. 2002; 87(2):845–858.

Fetsch CR, Odean NN, Jeurissen D, El-Shamayleh Y, Horwitz GD, Shadlen MN. Focal optogenetic suppression in macaque area MT biases direction discrimination and decision confidence, but only transiently. eLife. 2018 07; 7:E7297. doi: 10.7554/elife.36523.

Freedman DJ, Assad JA. Experience-dependent representation of visual categories in parietal cortex. Nature. 2006; 443(7107):85–8. http://www.ncbi.nlm.nih.gov/pubmed/16936716, doi: 10.1038/nature05078.

Freedman DJ, Assad JA. A proposed common neural mechanism for categorization and perceptual decisions. Nature Neuroscience. 2011 01; 14(2):143. http://www.nature.com/neuro/journal/v14/n2/full/nn.2740.html, doi: doi:10.1038/nn.2740.

Ganguli S, Bisley JW, Roitman JD, Shadlen MN, Goldberg ME, Miller KD. One-dimensional dynamics of attention and decision making in LIP. Neuron. 2008 04; 58(1):15 – 25. http://linkinghub.elsevier.com/retrieve/pii/S0896-6273(08)00168-2, doi: 10.1016/j.neuron.2008.01.038.

Gnadt JW, Andersen RA. Memory related motor planning activity in posterior parietal cortex of macaque. Experimental brain research Experimentelle Hirnforschung Experimentation cerebrale. 1988; 70(1):216–20. http://www.ncbi.nlm.nih.gov/pubmed/3402565.

Gold JI, Shadlen MN. The neural basis of decision making. Annual review of neuroscience. 2007; 30:535–74. http://www.ncbi.nlm.nih.gov/pubmed/17600525, doi: 10.1146/annurev.neuro.29.051605.113038.

Hanks TD, Mazurek ME, Kiani R, Hopp E, Shadlen MN. Elapsed decision time affects the weighting of prior probability in a perceptual decision task. J Neurosci. 2011; 31(17):6339–6352. doi: 10.1523/JNEUROSCI.5613-10.2011.

Hays AV Jr, Richmond BJ, Optican LM. Unix-based multiple-process system, for real-time data acquisition and control. WESCON Conf Proc. 1982 1; https://www.osti.gov/biblio/5213621.

Hernández A, Zainos A, Romo R. Temporal evolution of a decision-making process in medial premotor cortex. Neuron. 2002 03; 33(6):959 – 972.

Hikosaka O, Wurtz RH. Visual and oculomotor functions of monkey substantia nigra pars reticulata. III. Memory-contingent visual and saccade responses. Journal of Neurophysiology. 1983; 49(5):1268–1284. doi: 10.1152/jn.1983.49.5.1268.

Horwitz GD, Batista AP, Newsome WT. Direction-selective visual responses in macaque superior colliculus induced by behavioral training. Neuroscience letters. 2004; 366(3):315–319.

Kang YH, Loffler A, Jeurissen D, Zylberberg A, Wolpert DM, Shadlen MN. Multiple decisions about one object involve parallel sensory acquisition but time-multiplexed evidence incorporation. Elife. 2021; 10. https://www.ncbi.nlm.nih.gov/pubmed/33688829, doi: 10.7554/eLife.63721.

Kiani R, Hanks TD, Shadlen MN. Bounded integration in parietal cortex underlies decisions even when viewing duration is dictated by the environment. The Journal of neuroscience. 2008; 28(12):3017–29. http://www.ncbi.nlm.nih.gov/pubmed/18354005, doi: 10.1523/JNEUROSCI.4761-07.2008.

Kim JN, Shadlen MN. Neural correlates of a decision in the dorsolateral prefrontal cortex of the macaque. Nature neuroscience. 1999; 2(2):176–85. http://www.ncbi.nlm.nih.gov/pubmed/10195203, doi: 10.1038/5739.

King JR, Dehaene S. Characterizing the dynamics of mental representations: the temporal generalization method. Trends in cognitive sciences. 2014; 18(4):203–210.

Kremkow J, Jin J, Wang Y, Alonso JM. Principles underlying sensory map topography in primary visual cortex. Nature. 2016; 533(7601):52–57.

de Lafuente V, Jazayeri M, Shadlen MN. Representation of accumulating evidence for a decision in two parietal areas. J Neurosci. 2015; 35(10):4306–18. https://www.ncbi.nlm.nih.gov/pubmed/25762677, doi: 10.1523/JNEUROSCI.2451-14.2015.

Latimer KW, Yates JL, Meister MLR, Huk AC, Pillow JW. Single-trial spike trains in parietal cortex reveal discrete steps during decision-making. Science (New York, NY). 2015 07; 349(6244):184 – 187. http://www.sciencemag.org/content/349/6244/184.full.pdf, doi: 10.1126/science.aaa4056.

Lewis JW, Van Essen DC. Corticocortical connections of visual, sensorimotor, and multimodal processing areas in the parietal lobe of the macaque monkey. J Comp Neurol. 2000; 428(1):112–37. https://www.ncbi.nlm.nih.gov/pubmed/11058227, doi: 10.1002/1096-9861(20001204)428:1<112::aid-cne8>3.0.co;2-9.

Liu LD, Pack CC. The contribution of area MT to visual motion perception depends on training. Neuron. 2017; 95(2):436–446.

Lorteije JA, Zylberberg A, Ouellette BG, De Zeeuw CI, Sigman M, Roelfsema PR. The formation of hierarchical decisions in the visual cortex. Neuron. 2015; 87(6):1344–1356.

Mazurek ME, Roitman JD, Ditterich J, Shadlen MN. A role for neural integrators in perceptual decision making. Cerebral cortex (New York, NY : 1991). 2003; 13(11):1257 – 1269.

Meister MLR, Hennig JA, Huk AC. Signal Multiplexing and Single-Neuron Computations in Lateral Intraparietal Area During Decision-Making. Journal of Neuroscience. 2013 02; 33(6):2254 – 2267. doi: 10.1523/jneurosci.2984-12.2013.

Newsome WT, Britten KH, Movshon JA. Neuronal correlates of a perceptual decision. Nature. 1989; 341(6237):52–4. https://www.ncbi.nlm.nih.gov/pubmed/2770878, doi: 10.1038/341052a0.

Pachitariu M, Kilosort 2.0; 2021. https://zenodo.org/record/4147288.

Pachitariu M, Steinmetz N, Kadir S, Carandini M, D HK. Kilosort: realtime spike-sorting for extracellular electrophysiology with hundreds of channels. bioRxiv. 2016; p. 061481. doi: 10.1101/061481.

Paré M, Wurtz RH. Monkey Posterior Parietal Cortex Neurons Antidromically Activated From Superior Colliculus. Journal of Neurophysiology. 1998 01; 78(6):3493–3497. doi: 10.1152/jn.1997.78.6.3493.

Peixoto D, Verhein JR, Kiani R, Kao JC, Nuyujukian P, Chandrasekaran C, Brown J, Fong S, Ryu SI, Shenoy KV, et al. Decoding and perturbing decision states in real time. Nature. 2021; 591(7851):604–609.

Platt ML, Glimcher PW. Neural correlates of decision variables in parietal cortex. Nature. 1999 07; 400(6741):233 – 238. http://www.nature.com/nature/journal/v400/n6741/abs/400233a0.html, doi: 10.1038/22268.

Ratcliff R, Rouder JN. Modeling response times for two-choice decisions. Psychological science. 1998; 9(5):347–356.

Roitman JD, Shadlen MN. Response of neurons in the lateral intraparietal area during a combined visual discrimination reaction time task. The Journal of neuroscience. 2002; 22(21):9475–89. http://www.ncbi.nlm.nih.gov/pubmed/12417672.

Romo R, Hernandez A, Zainos A. Neuronal Correlates of a Perceptual Decision in Ventral Premotor Cortex. Neuron. 2004 01; 41(1):165 – 173. doi: 10.1016/s0896-6273(03)00817-1.

Salzman CD, Murasugi CM, Britten KH, Newsome WT. Microstimulation in visual area MT: Effects on direction discrimination performance. Journal of Neuroscience. 1992; 12(6):2331–55.

Sarma A, Masse NY, Wang XJ, Freedman DJ. Task-specific versus generalized mnemonic representations in parietal and prefrontal cortices. Nature Neuroscience. 2016; 19(1):143 – 149. doi: 10.1038/nn.4168.

Schall JD. Neural basis of saccade target selection. Reviews in the neurosciences. 1995 1; 6(1):63–85. doi: 10.1515/revneuro.1995.6.1.63.

Sereno AB, Maunsell JH. Shape selectivity in primate lateral intraparietal cortex. Nature. 1998 10; 395(6701):500–3. doi: 10.1038/26752.

Shadlen MN, Britten KH, Newsome WT, Movshon JA. A computational analysis of the relationship between neuronal and behavioral responses to visual motion. The Journal of neuroscience : the official journal of the Society for Neuroscience. 1996 02; 16(4):1486 – 1510.

Shadlen MN, Kiani R. Decision making as a window on cognition. Neuron. 2013; 80(3):791–806. http://www.ncbi.nlm.nih.gov/pubmed/24183028, doi: 10.1016/j.neuron.2013.10.047.

Shadlen MN, Newsome WT. Motion perception: seeing and deciding. Proceedings of the National Academy of Sciences of the United States of America. 1996; 93(2):628–33. http://www.ncbi.nlm.nih.gov/pubmed/8570606.

Shushruth S, Mazurek M, Shadlen MN. Comparison of Decision-Related Signals in Sensory and Motor Preparatory Responses of Neurons in Area LIP. J Neurosci. 2018; 38(28):6350–6365. https://www.ncbi.nlm.nih.gov/pubmed/29899029, doi: 10.1523/JNEUROSCI.0668-18.2018.

Silver MA, Kastner S. Topographic maps in human frontal and parietal cortex. Trends in Cognitive Sciences. 2009; 13(11):488–495. doi: 10.1016/j.tics.2009.08.005.

So N, Shadlen MN. Decision formation in parietal cortex transcends a fixed frame of reference. Neuron. 2022; 110:3206–3215.e5. doi: 10.1016/j.neuron.2022.07.019.

Stine GM, Zylberberg A, Ditterich J, Shadlen MN. Differentiating between integration and non-integration strategies in perceptual decision making. Elife. 2020; 9. https://www.ncbi.nlm.nih.gov/pubmed/32338595, doi: 10.7554/eLife.55365.

Stine GM, Trautmann E, Jeurissen D, Shadlen MN. A neural mechanism for terminating decisions. bioRxiv. 2022; https://www.biorxiv.org/content/10.1101/2022.05.02.490327v1, doi: 10.1101/2022.05.02.490327.

Stine GM, Trautmann E, Jeurissen D, Shadlen MN. A neural mechanism for terminating decisions. Neuron. 2023; in press.

Toth LJ, Assad JA. Dynamic coding of behaviourally relevant stimuli in parietal cortex. Nature. 2002 01; 415(6868):165 – 168. doi: 10.1038/415165a.

Trautmann EM, Hesse JK, Stine GM, Xia R, Zhu S, O'Shea DJ, Karsh B, Colonell J, Lanfranchi FF, Vyas S, et al. Large-scale brain-wide neural recording in nonhuman primates. bioRxiv. 2023; p. 2023–02.

Vyas S, Golub MD, Sussillo D, Shenoy KV. Computation through neural population dynamics. Annual Review of Neuroscience. 2020; 43:249–275.

Zhang Z, Yin C, Yang T. Evidence accumulation occurs locally in the parietal cortex. Nature Communications. 2022; 13(1):4426. doi: 10.1038/s41467-022-32210-6.

Extended Data

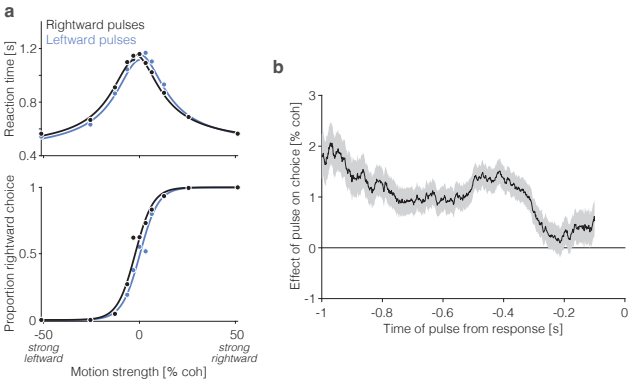

Figure S1. Effect of motion pulses on behavior (adapted from *Stine et al., 2023*). a, Choice (*bottom*) and reaction time (*top*) data as a function of motion strength from two monkeys, plotted separately for trials with leftward (grey) and rightward (black) motion pulses. Positive motion strengths represent leftward motion. The pulses (100 ms) had a biasing effect equivalent to shifting the choice function left or right by ± 1.4 % coh ($p < .001$, likelihood ratio test). **b,** Effect of motion pulses on choices as a function of time from the response. Pulses had a persistent effect on choices, consistent with temporal integration of motion evidence. Shading is ± 1 s.e.

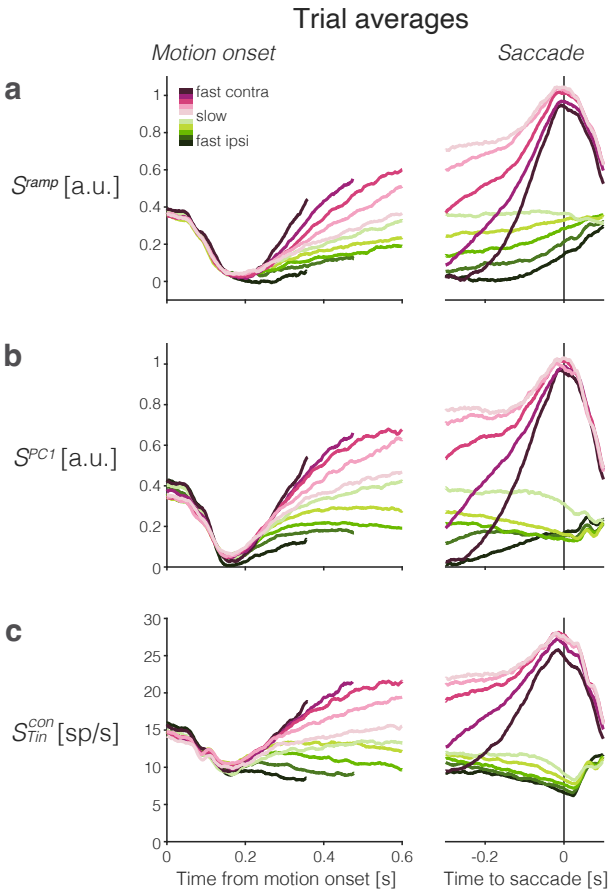

Figure S2. Trial-averaged activity grouped by RT quantile Rows show three types of population averages of single-trial responses. Choice and RT quantile are indicated by color (legend) and aligned to motion onset (left) and saccade initiation (right). **a,** Ramp coding direction. **b,** First principal component from PCA. **c,** Averages of the subset of neurons that have the left (contralateral) target in their response field. Correct and error trials are included in the both motion and saccade aligned averages.

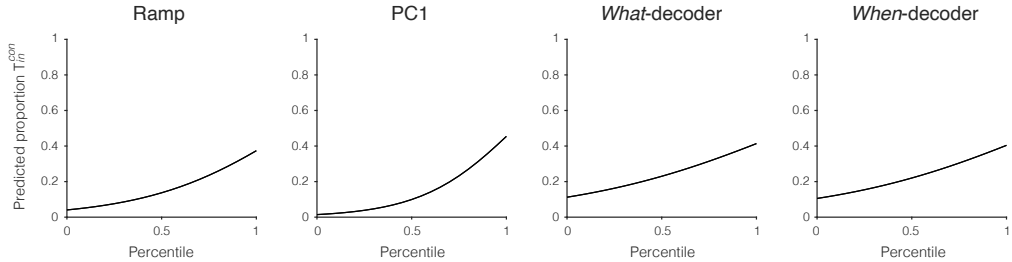

Figure S3. The T_{in} neurons are not discoverable by their weight assignments. The T_{in}^{con} neurons contribute strongly and positively to all coding directions, but they are a small fraction of the sampled population. Here we ask whether the rank of a neuron's weight might identify it as T_{in}^{con}. The graphs are logistic fits

$$P\left(I_k\right) = \frac{1}{1 + e^{-(\beta_0 + \beta_1 w_k)}}$$

to the binary variable

$$I_k = \begin{cases} 1 & \text{neuron}_k \in T_{in}^{con} \\ 0 & \text{otherwise.} \end{cases}$$

Neurons with stronger positive weights are more likely to be T_{in}^{con}, but even the largest weight percentile identifies a T_{in} neuron with a probability less than 0.4.

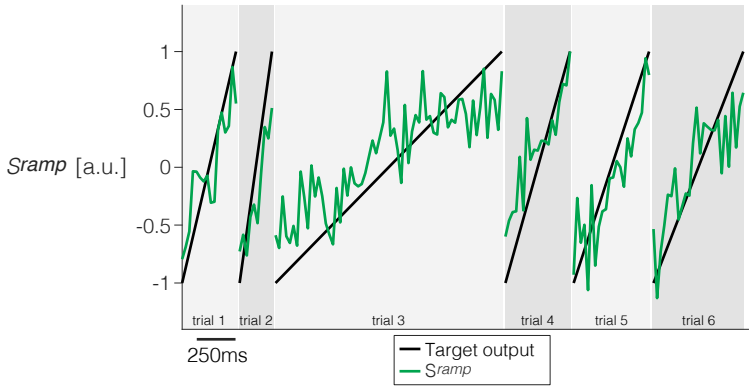

Figure S4. Derivation of a ramp coding-direction in neuronal state space. Weights are assigned to each of the N simultaneously recorded neurons in each session using simple least squares regression to approximate a ramp from -1 to $+1$ on the interval from 200 ms after motion onset to 100 ms before saccade initiation. Only trials ending in left (contraversive) choices are included. The graph shows the quality of the regression on 6 trials from Session 1. Projection of the population firing rates on the vector of weights renders the single trial signal, $S^{\text{ramp}}(t)$.

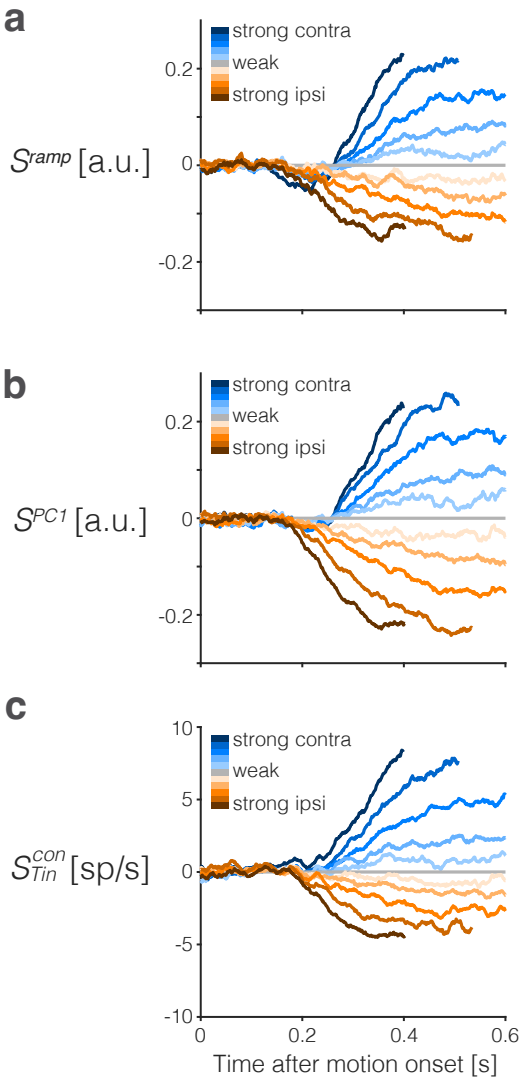

Figure S5. Trial-averaged activity after subtracting the urgency component. **a,** Ramp coding direction (S^{ramp})., **b,** PC1 (S^{PC1}). direction, **c,** Mean activity of $\mathrm{T}^{\mathrm{con}}_{\mathrm{in}}$ neurons ($S^{\mathrm{con}}_{\mathrm{Tin}}$). In all graphs, these are the same data as in Fig. 2, third column, after subtraction of the trace representing 0% coherence motion (gray).

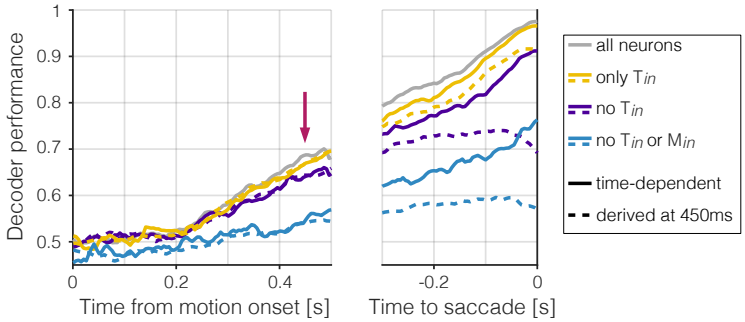

Figure S6. Decoding choice from subsets of neurons. Cross-validated, across-session mean accuracy of 7 choice decoders plotted as a function of time from motion onset (*left*) and time to saccadic choice (*right*). Solid traces indicate the accuracy of decoders trained at the time point at which they were evaluated (time-dependent). Dashed traces are generated by deriving decoder weights using only the activity at 450 ms from motion onset (red arrow, same as Fig. 4a) and applying these same weights at all other time points (*fixed training-time*). Trace colors indicate whether the decoders were trained using the activity of all neurons (gray), only T_{in}^{con} and T_{in}^{ips} neurons (yellow), all but T_{in} neurons (purple), or all but T_{in} and M_{in} neurons (blue). Decoding accuracy is greatly diminished without the contribution of these task-related neurons, which constitute only $28 \pm 1.7\%$ of the population (mean $\pm$ s.e.).

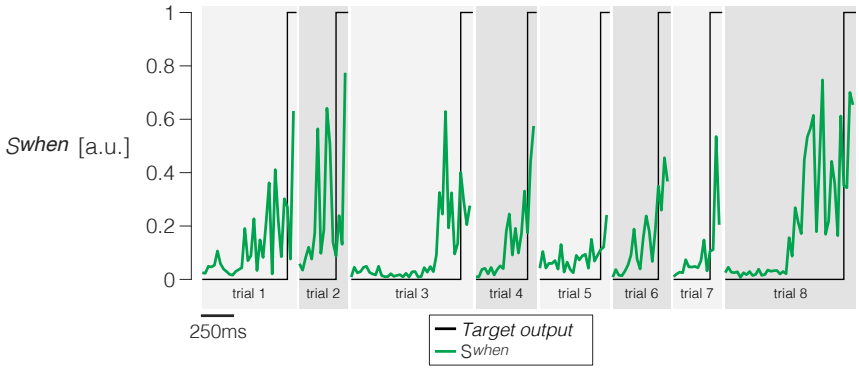

Figure S7. Derivation of a *When* direction in neuronal state space. Weights are assigned to each of the N simultaneously recorded neurons in each session using logistic regression to approximate a step that takes a value of 0 from 200 ms before motion onset to 150 ms before saccade initiation, and a value of 1 for the following 100 ms (the last 50 ms before the saccade are discarded). Only trials ending in left (contraversive) choices are included. The graph shows the quality of the regression on 8 example trials. The traces are shown from 200 ms after motion onset to 50 ms before the saccade. Projection of the population firing rates on the vector of weights renders the single trial signal, $S^{\mathrm{When}}(t)$.

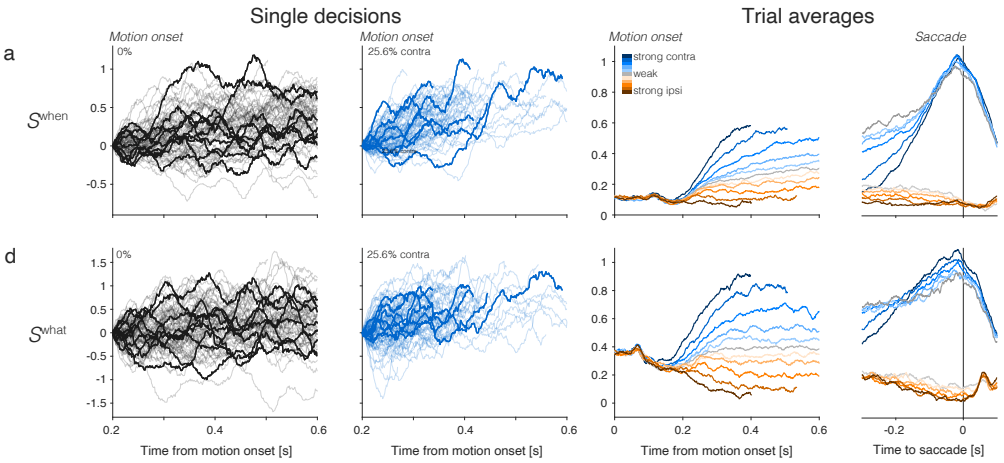

Figure S8. Single-trials and trial averaged signals furnished by the When- and What-decoders. Same convention as Fig. 2, using the same single-trial examples.

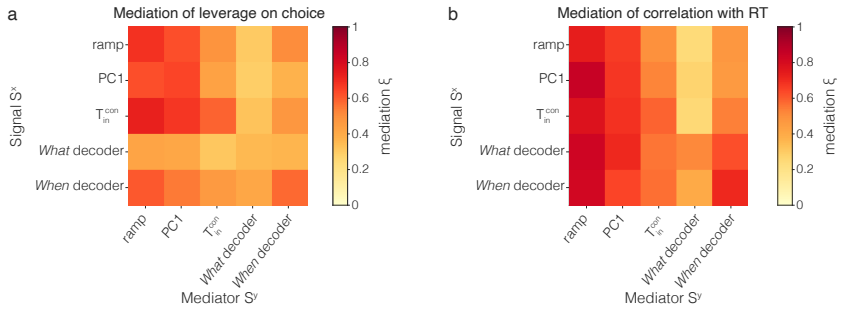

Figure S9. Cross-mediation of Single-trial correlations with behavior. The figure extends the observations in Fig. 5 that a sample of $S^{\text{con}}_{\text{Tin}}$ at $t = 550$ ms after motion onset (i) reduces the leverage of earlier samples of $S^{\text{con}}_{\text{Tin}}$ on choice and RT (mediation of S^x on S^x) and (ii) also reduces the leverage of earlier samples of other signals, S^{PC1} and S^{ramp} (cross-mediation of S^x on S^y). The The heatmaps are 5×5 matrices of the mediation indices, ξ^{Ch} and ξ^{RT}, (Eqs. 6 and 9), that is how a signal at $t = 550$ms mediates a signal at $t = 400$ ms after motion onset. The index is zero if there is no mediation by the later sample; one of the mediation is complete. The main diagonal (top left to bottom right) shows the mediation of S^x (0.55) on S^x (0.4). Values below the diagonal show cross-mediation of S^y by S^x; values above the diagonal show mediation of S^x by S^y. **a,** Leverage on choice. **b,** Leverage on RT. Notice that the matrices are not symmetric. For example, S^{ramp} mediates the leverage of $S^{\text{con}}_{\text{Tin}}$ on choice more $S^{\text{con}}_{\text{Tin}}$ mediates the leverage of S^{ramp}, and $S^{\text{con}}_{\text{Tin}}$ mediates the leverage of S^{When} on RT more than S^{When} mediates the leverage of $\text{T}^{\text{con}}_{\text{in}}$.